University of Alberta

Static and Dynamic Performance Evaluation of a Piezoresistive Silicon MEMS Strain Sensor

by

Ronald Delos Reyes

A thesis submitted to the Faculty of Graduate Studies and Research
in partial fulfillment of the requirements for the degree of

Master of Science

in

Materials Engineering

Department of Chemical and Materials Engineering

To Glenda, and our Gabrielle

ABSTRACT

Static and dynamic characterization was performed on a prototype piezoresistive silicon MEMS strain sensor. Static tests showed the MEMS sensor's gauge factor ranged from 10-13, which is higher than a foil gauge's gauge factor. Power measurements at -20 ^{o}C, 24 ^{o}C, and 80 ^{o}C showed that the average sensor power decreases as temperature increases. A dramatic decrease in the sensor voltage settling time was observed at a temperature of -20 ^{o}C. Sensor dynamic outputs measured at 10 Hz, 63 Hz and 175 Hz revealed noise in the signal and were processed using a digital low pass filter. Rainflow counting on the resulting strain histories revealed that the filtered MEMS sensor signal gives a conservative fatigue life estimate while the unfiltered MEMS signal overestimates the number of loading cycles. Extended vibration testing results showed that the sensor lifetime is 2.70 million cycles at an equivalent strain range of 1261 $\mu\varepsilon$.

ACKNOWLEDGEMENT

The author would like to express his deepest appreciation to the following who contributed in one way or another in making this successful thesis:

To the author supervisors: Professors Kenneth Cadien and Michael Lipsett, for their guidance, patience and encouragement. To Bernie Faulkner, Rick Conrad and Dr. Jilu Feng, for the technical assistance they extended in the conduct of some of the critical experiments. To Terry Wang of Scanimetrics, who gave crucial help with the rainflow cycle counting. To Dr. Sirish Shah, the author’s professor in the CHE 573 course from which much of the materials learned were used extensively in processing data from the dynamic measurements.

To the author’s parents: Edilberto and Priscila, for coming all the way from the Philippines to help in taking care of Gabrielle so the author can focus in his coursework requirements. To the author’s little bundle of joy, Gabrielle for being a constant source of inspiration and motivation, together with her mother. To Glenda, for her love and understanding especially the help she extended to the author in finishing the requirements along the way, from the coursework assignments up to editing the draft of the thesis manuscript. Without her, this thesis wouldn’t be a reality.

And last but not the least, to the greatest teacher and engineer of all: God almighty, for bestowing the author the gifts of wisdom, strength and perseverance, especially during the most challenging times. For these, this author offer Him his praise and thanks. May His name be glorified and praised always!

TABLE OF CONTENTS

LIST OF FIGURES

LIST OF TABLES

LIST OF SYMBOLS AND ABBREVIATIONS

ASTM E-251-92	American Society for Testing and Materials Standard Test Methods for Performance Characteristics of Metallic Bonded Resistance Strain Gauges
MEMS	micro-electro-mechanical systems
MTS	materials testing system machine

b	for a cantilever beam, refers to the beam`s width, measured in centimeters or millimeters
c	for a cantilever beam, refers to the distance of the beam surface from the beam's neutral plane. Typically equal to the half of the beam's thickness and measured in centimeters or millimeters
E	refers to Young's modulus of elasticity; the ratio of the applied stress on a material and the resulting deformation or strain
I	for a cantilever beam, refers to the beam`s cross section moment of inertia
K	sensor gauge factor; the ratio of the unit change in sensor resistance and the applied strain
L	symbol for the quantity length; also denotes length of a test specimen during the application of a certain level of strain
L_0	refers to original length of a test specimen or the specimen`s length at 0 strain
L_B	for a cantilever beam, refers to the beam length; measured in centimeters or millimeters
M	for a cantilever beam, refers to the resulting bending moment when a force P is acting on its free end, measured in units of newton-meters (N-m)
P	for a cantilever beam, refers to the bending force applied to the beam's free end. Measured in units of newtons
R	refers to the sensor resistance; also denotes measured resistance during the application of a certain level of strain
R_0	initial sensor resistance, or sensor resistance measured at 0 strain
S	refers to the sensor sensitivity which is the amount of voltage change during the application of a certain amount of strain, S = $\Delta V/\varepsilon$ usually measured in units of millivolts/microstrains (mV/με)
t	for a cantilever beam, refers to the beam's thickness, measured in centimeters or

millimeters

V	refers to sensor voltage measured during the application of a certain amount of strain
V_0	refers to the original sensor voltage or simply the sensor voltage measured during 0 strain
x	for a cantilever beam, refers to any position in the beam measured longitudinally from the beam's free end, measured in centimeters
Δ	denotes difference between quantities measured before and during the application of strain e.g. ΔR denotes the difference $R - R_0$
δ	for a cantilever beam, refers to the deflection of the beam's free end when a localized force acts on the beam's free end; measured in centimeters or millimeters
ε	refers to strain which is the unit change in the length of an object during the application of a force which causes deformation. For convenience, measured in units of microstrains
$\mu\varepsilon$	refers to the unit of microstrain, defined as the 1×10^{-6} of a strain, or 0.0001% change in the original length of a material
σ	symbol for the quantity stress which is related to strain by Hooke's Law; in metric system, measured in terms of pascals (N/m^2)

Chapter 1

INTRODUCTION

Equipment or structures under vibration are subject to varying stress and strains which contribute to damage [1]. Dynamic loading and random vibrations promote material fatigue which eventually will lead to failure. To maintain reliable operation, condition monitoring of equipment is needed. This task is commonly accomplished by using bonded resistance strain gauges, which consist of a grid-patterned metallic foil filament encapsulated in a polymer carrier material. From the initial development by Simmons and Ruge in 1938 [2] and further refinement by Jackson [3], the foil strain gauge has been used extensively for static and dynamic strain measurements [4-5], force and torque measurements [6] and structural health monitoring [7]. The foil strain gauge is bonded to a specimen under strain, thus the strain experienced by the specimen is directly transferred into it. This strain is detected as a change in the electrical resistance of the foil strain gauge. However, foil strain gauges work best at room temperature. At extreme temperatures, the change in the foil strain gauge resistance is not linear. This limits the performance of the strain gauge to room temperature applications, making applications in extreme environments a challenge.

An alternative device that can address the limitation posed by metallic foil strain gauges is the semiconductor strain sensor. The electrical resistance of a semiconductor, similar to the foil strain gauge, changes when it is subjected to strain. This semiconductor property known as piezoresistance is well known in silicon [8-12]. Single-crystal silicon, aside from having desirable electronic properties, also has good mechanical properties

[13]. The combined good mechanical and electronic properties of silicon made it an important and practical choice of material for strain sensors and other micro-electro-mechanical system (MEMS) sensors [14] such as accelerometers [15], microcantilever force sensors [16] and pressure sensors [17]. Silicon is in majority of the today's commercial microelectronic devices. This can be attributed to the fact that raw silicon in the form of sand (SiO_2) is cheap and abundant; and the microfabrication and nanofabrication techniques used in the manufacture of electronic devices from silicon have been well established [18]. Manufacture of MEMS devices developed from silicon microfabrication technology which relies heavily on precise bulk silicon micromachining processes [19]. Microfabrication of silicon piezoresistive MEMS strain sensors offer advantages [20] such as device miniaturization, integration with sensor microelectronics, and mass production.

In addition, silicon strain sensors have been reported to have excellent response to strain, due to large resistance change with applied strain [21]. The ratio of the unit change in sensor resistance with applied strain is known as the sensor's gauge factor and is used to describe a sensor's strain sensing capability. Silicon strain sensors typically have higher gauge factors than conventional foil strain gauges. Temperature has minimal effect on the sensor's gauge factor. Silicon strain sensors also have higher resistance and consume less power, thus making it compatible with battery operated modules for wireless data acquisition systems. It is also reported that silicon strain sensors have superior fatigue lifetime, lower hysteresis and better strain-response linearity [22].

However, silicon strain sensors are still in continuous development. A great deal of recent work [23-29] is focused mainly on design and optimization with the principal motivation of creating a prototype sensor having better sensitivity and performance than existing foil strain gauges. Performance characterization carried out in these studies are less than complete since procedures adapted probe only the static strain response while sensor dynamic response is mostly left out. The dynamic sensor response is one area of importance since fatigue damage is estimated using strain history obtained from strain sensors. Moreover, there is a need to evaluate piezoresistive silicon strain sensor's performance reliability in extreme conditions such as extreme strain, high frequency vibration and low temperatures since these conditions promote yield, fatigue, fracture and eventual material failure. Addressing both static and dynamic response, as well as performance under extreme conditions will therefore give a more complete description of the sensor's performance and its capabilities.

Chapter 2

REVIEW OF THE STATE OF THE ART

Silicon is the single most important material for modern solid state electronics and MEMS devices because of its desirable electronic and mechanical properties and adaptability to different micromachining techniques. Although perceived as a brittle material, it has been reported that single crystal silicon material exhibits very good mechanical properties comparable to common engineering materials [21]. Its Young's modulus of elasticity is almost approaching that of steel, and its yield strength is higher than those of some common metals such as aluminum, tungsten and stainless steel. In addition, processing steps to form oxides (SiO_2) and nitrides (Si_3N_4) with silicon are known to improve its strength and other mechanical properties.

The discovery of silicon piezoresistive property in 1954 [30] generated great interest in using silicon for mechanical sensing applications [31]. With excellent electrical response to applied strain, silicon was found to be ideal for use in strain sensors. As devices geared towards higher performance and miniaturization in the microelectronics industry, silicon micromachining [19, 32] processes were improved. This aided the development of next-generation class of devices known as piezoresistive silicon MEMS sensors where the sensing elements were formed by impurity doping of silicon. Piezoresistive silicon MEMS sensors have been used as strain sensors, pressure sensors, accelerometers and cantilever force sensors. Among these, silicon MEMS strain sensors were given a great attention because they were considered as a possible replacement to metal-foil gauge sensor. Silicon MEMS strain sensors were reported to have better sensitivity and 10-100 times higher gauge factor value than metal-foil strain gauges [22-26]. The improved sensor sensitivity and performance from using silicon is seen as the driving motivation for continuous development of prototype strain sensors. However, test procedures based on accepted standards are required to analyze and verify the claim for improved performance of prototype sensors to ensure reliability of results.

Another strong motivation for adapting the silicon MEMS strain sensors over the conventional strain gauge is device integration. Microfabrication has enabled strain sensor integration with electrical components [23-26, 29, 43, 46-48] resulting to miniaturization of the device. Along with miniaturization, sensors with integrated components were able to accomplish reduction in power consumption [33]. This reduction in power consumption makes the integrated sensor suitable for battery-powered wireless data acquisition.

Parkins [34] and Mason [35] reported procedures on calibration of early semiconductor strain sensors. These semiconductor strain sensors are grid-patterned polysilicon, similar to the present metal-foil strain gauge, and largely different from today's integrated silicon MEMS strain sensors. These procedures preceded the standard protocol for bonded resistance strain gauge testing, the ASTM E-251-92 [36] which was developed in 1984 and last updated in 2009. Recent prototypes of silicon strain sensor use this standard as a reference for testing since the pertinent strain gauge characteristics and performance characterization steps it defines are also applicable to silicon strain sensors. One test method described in the standard that is highly adaptable to silicon strain sensor testing is the constant-stress cantilever beam method. Sensor sensitivity and response is readily demonstrated using a simple static bending test with a constant stress cantilever beam. With this technique, voltage-to-strain measurements using the same test specimens can be performed several times to test for repeatability during calibration. For regular strain gauges and metallic strain sensors [37], this technique is able to combine temperature dependent-static strain measurements in order to determine sensor sensitivity and temperature coefficient of resistance. Another advantage is that it can also be used to carry out sensor dynamic testing and calibration as reported by Donohoe et al. [38]. Free vibration on a test beam was initiated using a mechanical impulse from a linear actuator which was able to excite the beam's first few resonant frequencies. Temperature response of the sensor was also characterized from 30 ^{o}C to 80 ^{o}C by incorporating an environmental chamber into the dynamic test set-up. Though the sensor dynamic response was successfully tested, the performance under extended or random vibration wasn't reported.

Instead of the constant stress cantilever beam, a number of silicon strain sensor prototypes [39-45] adapted the simpler rectangular cantilever beam for testing the sensor performance. The microfabricated strain sensors used static strain inputs for testing. Results show excellent sensor strain sensitivities which are better than those reported for conventional metal-foil strain gauges. Several works [23, 45] have further reported on successful measurement of the sensor temperature coefficient of resistance. They found a very small change in the sensor resistance for temperatures tested between 25 ^{o}C and 130 ^{o}C, indicating thermal stability of the prototype silicon strain sensors. Despite the success of this method in characterizing the excellent response of silicon strain sensors, the sensor evaluation presented was far from complete as the results reported were limited to static strain response. The test procedures used were not extended to include vibration testing that will have effectively described the sensor dynamic response.

Aside from the cantilever method, an alternative way to determine sensor response is the direct tension method [36]. This technique makes use of the strain produced in a test bar specimen by applying direct tensile load on the bar. The input strain is applied quasi-statically while the sensor voltage output is being monitored. The method was successfully used in temperature dependent measurements as demonstrated by Mohammed et al[46] in testing a prototype sensor in the temperature ±50 ^{o}C range; and by Won et. al. [47] wherein sensor performance was determined in the temperature range of 40 to 80 ^{o}C. The prototype sensors tested showed enhanced sensitivity and low thermal drift in sensor resistance. A limitation of this method is that the input strain is purely tensile (or compressive in some cases), thus is not suitable for sensor dynamic testing. Evaluation results have successfully revealed silicon strain sensors to have excellent strain response, sensitivity, thermal stability and power consumption characteristics. Performance under extreme temperature conditions have tested for temperature as low as -50 ^{o}C, and at high temperatures exceeding 100 ^{o}C. Temperature dependent measurements have revealed that silicon strain sensors have good thermal stability, having minimal change in its sensitivity and electrical resistance. Power consumption reduction was also demonstrated as a result of sensor integration and miniaturization.

However, the reported strain performance was incomplete as it largely dealt only with static strain response, with no description of the sensor dynamic response. It has been shown that present test configurations of static testing can be extended to carry out dynamic testing by free vibration though it wasn't carried out all the time. In addition to dynamic testing, sensor performance under extreme vibrations such as high frequency vibrations and extended vibrations wasn't addressed as well. High frequency vibration and extended vibration testing provide a measure of the operational reliability of the strain sensor. The sensor performance under these conditions is of importance since the strain histories measured by the sensor under continuous vibration is used to calculate accumulated damage and fatigue lifetime estimates. Power consumption measurements, crucial to strain sensors in a wireless network, showed that silicon strain sensors are suitable as battery-operated devices. However, measurements failed to report on sensor voltage's settling time to input voltage. This parameter is important since longer or shorter voltage response time will have a direct impact on the sensor battery life. This parameter also has to be tested at different temperature extremes since strain sensors that operate as part of a wireless network are normally deployed on equipment operating outdoors, exposed to different environmental extremes.

Performance characterization and evaluation must be able to reveal the operational limits of the sensor in order to give a complete description of the device's reliability. Therefore, to describe the strain sensor performance, these limitations of the state of the art must be addressed. Thus, the following specific research objectives are set:

(1) Perform static strain testing and sensor voltage-to-strain calibration using procedures consistent with ASTM-E-251-92 standard.
(2) Determine sensor response at room temperature, as well as in extremes such as low temperature and high temperature. At the same time, the electrical

characteristics of the sensor such as power consumption and voltage settling time will also be determined.

(3) Obtain sensor dynamic response using vibration testing at low and high frequencies

(4) Determine sensor performance under extended vibration

Chapter 3

METHODOLOGY OF PROPOSED SOLUTION: THE ASTM E-251-92 AND THEORETICAL BACKGROUND

Prototype piezoresistive silicon MEMS strain sensors, with projected applications in heavy equipment vibration and fatigue monitoring in the oilsands industry were acquired by the Integrated Reliable Oilsands Systems Lab. The sensors, manufactured by Nemsor Inc., were obtained for reliability and performance testing. To give a complete evaluation of the characteristics and performance of the prototype MEMS strain sensors, the procedures from the ASTM E251-92 [36] standard were reviewed. In this section, the pertinent sensor characteristics and prescribed characterization set-ups identified by the standard as well as supplementary theoretical background are presented.

3.1 Sensor gauge factor

In calibrating the performance of a strain sensor, the primary sensor characteristic to be determined is the sensor gauge factor. The gauge factor K is the strain sensor's transfer function and defined as the ratio of the sensor's unit change in resistance with the applied strain

$$K = \frac{\frac{R - R_0}{R_0}}{\frac{L - L_0}{L_0}} = \frac{\frac{\Delta R}{R_0}}{\varepsilon} \qquad (3.1)$$

Another important parameter is the sensor sensitivity S defined as the ratio of the change in the sensor voltage, *ΔV* with the applied strain ε.

$$S = \frac{\Delta V}{\varepsilon} \qquad (3.2)$$

Empirically, the sensor voltage output, *V* varies directly proportional with the applied strain. Thus, the sensitivity can also be defined as the slope of the voltage vs. strain curve.

$$V(\varepsilon) = S\varepsilon + V(0) \qquad (3.3)$$

The sensor gauge factor can be calculated using the sensor sensitivity value. The DC current through the resistor is constant since the strain sensor is connected in series with the voltage source. For an ohmic sensor, the change in the sensor resistance as strain is applied is proportional to voltage change. Thus, the gauge factor can be expressed in terms of unit change in the voltage as:

$$K = \frac{\frac{\Delta V}{V_0}}{\varepsilon} = \frac{\Delta V}{V_0 \times \varepsilon} \qquad (3.6)$$

To determine the gauge factor of a strain sensor, the ASTM guide describes three equivalent procedures. These are (a) Constant bending-moment beam method (b)

Constant-stress cantilever beam method (c) Direct tension (compression) method. Among these methods, the constant-stress cantilever beam method is capable of repeatable tensile and compressive strain inputs.

3.2 Characterization set-up: Electrical components

The conventional method of detecting resistance change in a strain gauge during application of strain is by connecting it to standard resistors to form a Wheatstone bridge circuit. The Wheatstone bridge is formed by connecting in parallel two pairs of resistors that are in series connection as shown in Figure 1. In the figure, the series resistors R1 and R2 are in parallel with R3 and R4. If all the resistors have equal resistances, the voltage drop across the two arms (R1+R2 and R3+R4) will be zero.

If one resistor in the Wheatstone bridge is a strain gauge subject to strain, voltage imbalance between the two arms is created, which can be detected by the voltmeter. The amount of strain input into the strain gauge is proportional to the voltage imbalance detected by the voltmeter.

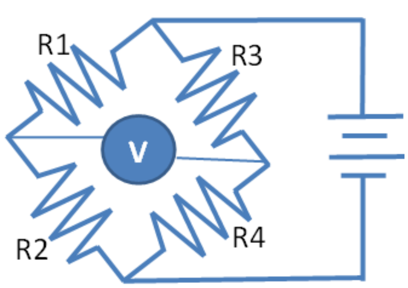

Figure 1: The Wheatstone bridge circuit

Depending on the desired accuracy and sensitivity, the strain gauge connection can be carried out in various ways. The simplest of which is the quarter bridge configuration where one strain gauge replaces a resistor in the bridge connection. A second method of detecting the strain-induced voltage change is by utilizing two strain gauges connected to two standard resistors, similarly known as the half-bridge configuration as shown in Figure 2. In this configuration, two strain gauges in series are installed on opposite sides of a test specimen, the second gauge being directly below the first. This configuration creates a better signal from the strain gauge connection since for an input strain, one sensor is under tension and the other one is under compression. The third method of connecting strain gauges is using two half bridge connections together to form a full-bridge. In a full bridge connection, all the resistors in the Wheatstone bridge circuit are replaced by strain gauges. In the case of cantilever test beam, the installation is done such that two of the strain gauges are under tension and the other two are under compression. Among these configurations mentioned, the full bridge connection has the best accuracy and sensitivity in detecting strain.

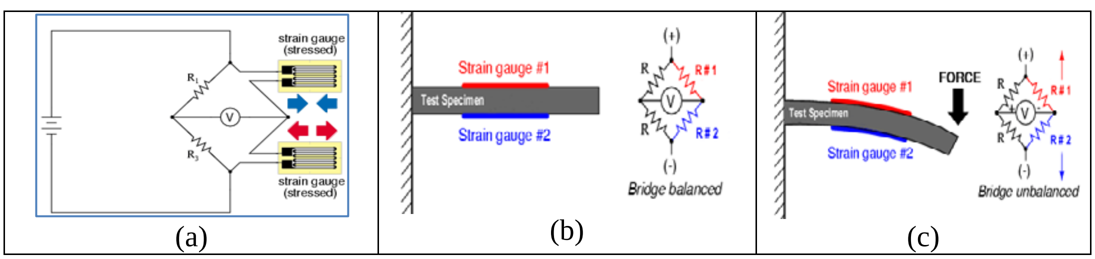

Figure 2: The half bridge connection. Figure 2a shows the schematic diagram for the half-bridge connection, using two foil gauges as resistors in the Wheatstone bridge. Figure 2b shows how the strain gauges are bonded onto a cantilever test beam. The strain gauges are bonded on both faces of the beam. For any longitudinal bending as shown in Figure 2c, one gauge is subject to strain (tension) while the other gauge is subject to the negative of that strain (compression) [49]

3.3 Characterization set-up: The cantilever beam

A cantilever beam test specimen allows for an effective method of calibration of a strain sensor. A good range of tensile and compressive strains can be created and repeated consistently by controlled deflections in the beam's free end. The deflections are measured with relative ease and precision i.e. using a Vernier caliper.

From beam theory, a rectangular cantilever beam shown in Figure 3 with a localized force on its free end will have a stress distribution which is linearly increasing from 0 to a maximum near the cantilever beam's fixed end. The position dependent stress σ(x) can be computed as

$$\sigma(x) = \frac{M(x) \cdot c}{I} = \frac{P \cdot x \cdot c}{I} \qquad (3.7)$$

Where:

M(x) is the position-dependent bending moment on the beam, given by the product of the localized force magnitude *P* and position *x*

c is half of beam thickness *t*, or the distance of the neutral axis to beam surface

I is the beam's area moment of inertia

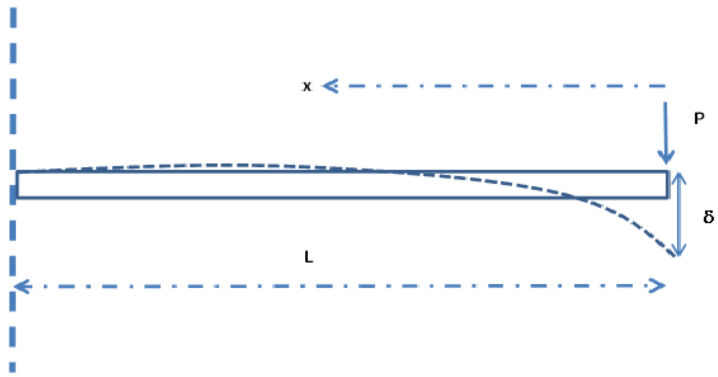

Figure 3: Schematic diagram of the cantilever beam deflection. P is the localized force acting on the free-end x = 0. The position dependent stress σ(x) is distributed along the length of the beam and increases with x. For any displacement δ of the beam`s free end, the stress is 0 at P's point of action and maximum at the base of the beam (x = L).

The stress-strain relation can be obtained by applying Hooke's Law. According to this law, the longitudinal strain *ε(x)* varies linearly also with position. The ratio of the stress and strain is the beam material's Young's modulus of elasticity *E*.

$$\sigma(x) = \varepsilon(x) \cdot E \tag{3.8}$$

For a beam with rectangular cross section of thickness *t* and width *b*, the area moment of inertia *I* is given by

$$I = \frac{bt^3}{12} \tag{3.9}$$

Substituting I in equation (3.9) to equation (3.7), the position dependent stress can be re-expressed as

$$\sigma(x) = \frac{6P \cdot x}{bt^2} \tag{3.10}$$

Now consider a rectangular beam with beam length L_B (to differentiate it from L, which is the length of a specimen under strain defined in equation 3.1), the deflection of the free end ($x = L_B$) is given by

$$\delta = \frac{P{L_B}^3}{3EI} \tag{3.11}$$

Substituting the expression for I will yield

$$\delta = \frac{4P{L_B}^3}{Ebt^3} \tag{3.12}$$

From equation (3.8), the stress-strain ratio at any point along the beam is always equal to Young's Modulus of elasticity E. Therefore the deflection of the beam free end in terms of stress is given by

$$\delta = \frac{4\varepsilon(L_B)P{L_B}^3}{\sigma(L_B)bt^3} \tag{3.13}$$

Using $x = L_B$ and applying equation (3.10), equation (3.13) can be rearranged as

$$\left(\frac{6PL_B}{bt^2}\right)\delta = \frac{4\varepsilon(L_B)P{L_B}^3}{bt^3} \tag{3.14}$$

If only one position is considered, e.g. $x = L_B$, the strain is only dependent on the deflection, δ. Hence, equation (3.14) can be simplified to get a deflection-dependent strain expression near the fixed end of the beam. The strain near the base of the beam is therefore given by

$$\varepsilon = \frac{3t\delta}{2{L_B}^2} \qquad (3.15)$$

Instead of a regular rectangular cantilever, the ASTM standard recommends a cantilever beam with modified shape, such that all the stress in the beam's surface is not dependent on position. Using two sensors each placed at the top and bottom of the beam allows measurement of tension and compression at the same time. Thus, the MEMS strain sensor response can be tested together with a standard foil strain gauge.

The beam can be modified such that its width increases constantly with its length. The beam width *b* can be described as $b = kx$, with *k* being a positive number such as in the case of a trapezoidal beam. If *b* is replaced with *kx* in equation (1), then the stress is given by

$$\sigma = \frac{6P}{kt^2} \qquad (3.16)$$

The length dependence of the stress is effectively eliminated. This type of beam therefore has constant stress in its surface for every load *P*. The strain can be calculated by equating the right hand side of equation (3.16) with equation (3.8), and expressing P in terms of equation (3.12). Take note that equation (3.12) dictates that $x = L_B$ thus the strain ε is constant and *b* is expressed as kL_B

$$\varepsilon \cdot E = \frac{6}{kt^2}\left(\frac{\delta E k L_B t^3}{4{L_B}^3}\right) \tag{3.17}$$

Simplifying this expression, we find the strain in a constant-stress cantilever beam similar to equation (3.15).

$$\varepsilon = \frac{3t\delta}{2{L_B}^2} \tag{3.18}$$

The difference with equation (3.18) is that it gives the strain value at any point in the surface of the trapezoidal area of the constant-stress cantilever beam when the free end of the beam is deflected. Thus by using a constant stress cantilever beam (Figure 4), the sensor can be tested accurately as long as it is located in the constant stress area and the stress and strain are only dependent on the displacement of the beam's free end.

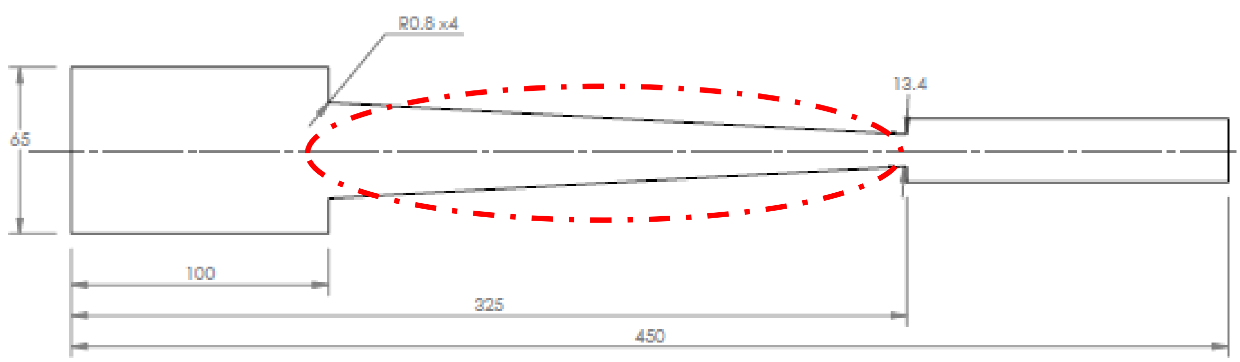

Figure 4: A constant stress beam used in the strain sensor testing. It makes use of the trapezoidal feature (region bounded by the ellipse) where surface stress the same for all points for a given load P or equivalently for any deflection of the free end. The dimensions shown are in millimeters.

3.4 Characterization set-up: Dynamic test apparatus

The dynamic test method described in the ASTM standard is intended for obtaining a metallic foil strain gauge’s gauge factor variation with temperature. This method utilizes a mechanism to produce vibration in a test beam specimen and an environmental chamber to create the background temperature where the strain gauge will operate. The method prescribes a motor driven cam or an electromechanical vibrator as means to produce constant amplitude vibrations on the cantilever beam specimen. The environmental chamber is equipped by radiant heaters in order to create high temperature conditions. A schematic diagram of the set-up is shown in Figure 5. This procedure is outlined since the resistance of a metallic foil gauge changes with variation in temperature, leading to a change in the gauge factor. For silicon MEMS strain sensors however, the resistance of a sensor is not strongly affected by changes in temperature. Removing the environmental chamber in the set-up, effective leaves a dynamic test rig which can be used to investigate sensor response under dynamic loading. Equivalent to a motor-driven cam, an electrodynamic shaker table can be used to produce base excitations on a cantilever test beam.

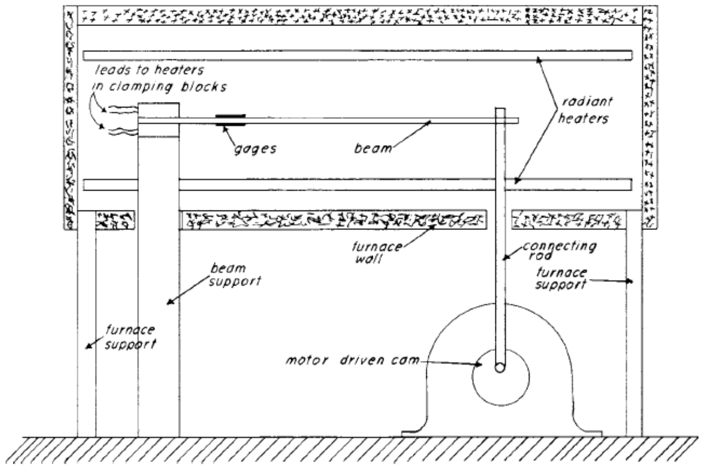

Figure 5: Schematic diagram of the ASTM set-up to determine sensor's gauge factor variation with temperature. In metallic foil gauges, the gauge factor is a function of temperature since the foil gauge's resistance changes with temperature [36]

On the other hand, the environmental chamber can be used with static bend test set-up to determine temperature effects on the sensor response. The environmental chamber described here is limited only to temperatures above 24 ^{o}C. Alternatively, in combination with a static test set-up the chamber can be replaced by a box furnace for high temperature measurements and a freezer for low temperature measurements.

Chapter 4

DESCRIPTION OF EXPERIMENTAL APPARATUS AND PROTOCOLS

From the general overview provided by the ASTM standard, specific procedures consistent with the standard were tailored to attain the specific research objectives. In this section, the experimental set-ups for the static testing, electrical switching characterization and dynamic testing are discussed in detail.

4.1 Description of the prototype strain sensors, installation and electrical conditioning

Typically for microfabricated silicon strain sensors, the wheatstone bridge circuit is integrated in the sensor's device chip. Similarly, the prototype sensor tested was designed to emulate a full-bridge strain gauge connection, having two wire leads for power/conditioning and another pair of leads for sensing as shown in Figure 6. Sensor fabrication procedure made use of a 5-mask microfabrication process flow similar to those described in [25-26, 46, 48]. The sensor was designed to perform over a range ± 2000 $\mu\varepsilon$ and ± 50 ^{o}C temperature.

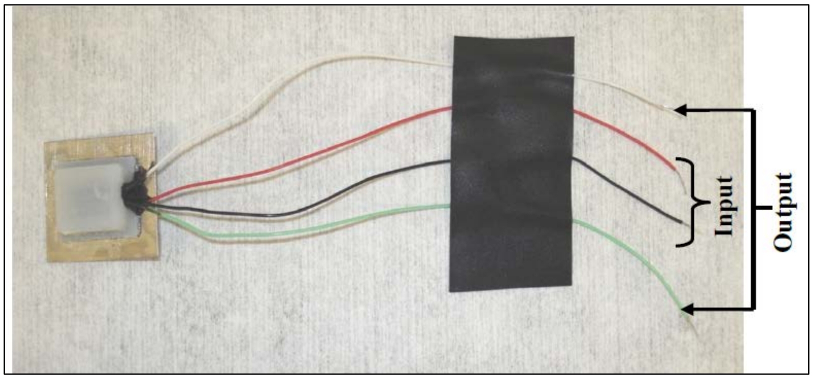

Figure 6: The prototype piezoresistive MEMS strain sensor. The sensor is bonded onto 16 gauge steel shims for easy installation on test beam specimens. The sensor has two leads for power (input) and another two leads for sensing (output)

The sensor installation used procedures similar to bonding conventional strain gauges. The initial step was modification of the metal surface by sanding, using SiC sandpaper. Then, surface cleaning and degreasing was done with an application of alcohol. Next, the surface was applied with a conditioner light etchant diluted phosphoric acid. Then, ammonium hydroxide was applied to neutralize the acid from the previous step and render the surface electrically neutral. Lastly, the catalyst and the cyanoacrylate adhesive (Micro-Measurements M-bond 200) were applied prior to putting the surfaces in contact with each other. The MEMS sensor was clamped down for about two minutes to ensure good contact as the adhesive cured and set in. A reference Micro-Measurements 8 mm x 5 mm electroresistive strain gauge (CEA-13-0620W-350) was also installed on the underside of the test beam, directly below the MEMS strain sensor. The strain gauge has a resistance of 350 Ω and gauge factor of 2.17 ± 0.5%. Sensor signal conditioning used a 2-channel Vishay 2110 variable voltage source. Excitation was done according to the manufacturer’s recommendation. The strain gauge was excited at 5.0 V while the MEMS sensor was at 3.0 V. The strain gauge was connected in a quarter bridge configuration, while the MEMS sensor was wired up similar to a full bridge connection.

4.2 Static Testing – Direct tension method and Constant-stress cantilever beam method

Initial direct tension testing, shown in Figure 7, was carried out using a 20.0 cm x 1.95 cm x 0.30 cm rectangular steel bar on a Materials Testing System (MTS) machine. The direct tension method uses a uniaxial tensile strain to determine the strain range at which the MEMS sensor response is linear before the onset of any failure. The MTS machine was programmed to apply a uniformly increasing uniaxial tensile strain on the test bar. Change in the test bar's length was monitored by an MTS extensometer, from which the real-time strain input can be determined. The MEMS sensor is excited at 3.0 V using the Vishay 2110 signal conditioner. The responding MEMS sensor voltage and the extensometer's measurements were captured and recorded by the MTS machine's built-in data acquisition system.

Figure 7: Uniaxial direct tension testing on a MTS machine of the MEMS strain sensor, installed in a steel test bar. This procedure was performed to investigate the strain limit of the MEMS strain sensor

For the constant-stress cantilever beam method, static bending tests were performed on a constant-stress beam test specimen, similar to that shown in Figure 4. The test beam was fabricated from a 1/8-inch aluminum sheet using a water jet cutter. The beam was assembled into a cantilever in the bed of a milling machine, supported by steel blocks. Controlled deflections of the test beam's free end were performed using a Friedrich Deckel Munchen FP-1 milling machine (Figure 8). The beam deflections ranged from 0 to 16.7 mm, corresponding to a strain range of 0 to 1400 $\mu\varepsilon$. Deflection steps were in increments of 100 $\mu\varepsilon$. The strain range was chosen such that it stays within the elastic limit of the aluminum test specimen. A Vishay 2110 strain gauge conditioner was used to excite the MEMS sensor at 3.0 V, and the reference strain gauge at 5.0 V. Voltage outputs from the MEMS sensor and the strain gauge were measured using an Agilent U1232A digital multimeter

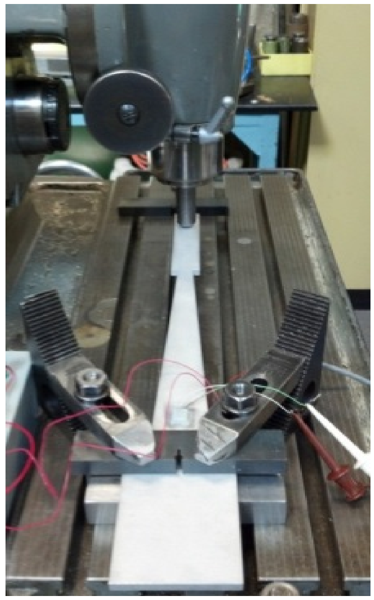

Figure 8: Constant-stress cantilever beam bend testing set-up in the bed of a Friedrich Deckel Munchen FP-1 milling machine. The test beam is assembled into a cantilever using steel blocks for support.

4.3 Sensor electrical and switching characterization

Sensor voltage settling time during switch-on/switch-off events, and how these responses vary with temperature was investigated. Sensor V-I characteristics were also determined using the set-up shown in Figure 9. For this purpose, a scaled down version of the constant-stress beam was fabricated and used on a custom-built table top bend-test module shown in Figure 10. The test beam, with length of 30 cm, was installed as a cantilever in the bend test module. Using a screw, small deflections were made in the beam free end and were measured by a vernier caliper. The sensor was wired up to the Vishay 2021 variable voltage source for conditioning with the sensor current being monitored by a high impedance Agilent U1232A digital multimeter. The sensor voltage response during switch-on and the corresponding voltage rise-time/fall-time was measured using TPS 2012 Tektronix digital storage scope operating in single-shot capture mode. The trigger was set as half of the maximum sensor voltage output. The rise time corresponds to the time it took the sensor voltage to go from 0 to 90% of the maximum voltage during a switch-on event. The fall time corresponds to the time it took for the sensor voltage to go from 100% to 10% of the maximum voltage during a switch-off event. The measurements were acquired for loaded (strained) and unloaded (unstrained) cases. The loaded case has a deflection of 15.00 mm on the cantilever free end, equivalent to 221 $\mu\varepsilon$. These measurements were carried out at room temperature (24 ^{o}C), low temperature (-20 ^{o}C) and high temperature (80 ^{o}C) to probe any variation on sensor voltage response with temperature. According to the ASTM standard, the allowed temperature fluctuation during testing is within ±2.0 ^{o}C of the reference temperature. A Fluke 52-2 dual input thermometer with type-K thermocouple was used to monitor the temperature. In the absence of an environmental chamber capable of creating both high and low temperature environments, the low temperature measurements were carried out in a walk-in freezer storage facility of the Department of Earth and Atmospheric Sciences, University of Alberta. The low temperature measurements were performed at -20 ^{o}C, which is the lowest stable temperature attainable by the freezer. The high temperature measurements were done using a Hotpack Supermatec box-type furnace in the Mechanical Engineering Machine shop. High temperature measurements were limited to 80 ^{o}C to ensure that the adhesive used for sensor bonding will be stable since adhesive melting can have an onset near 100 ^{o}C.

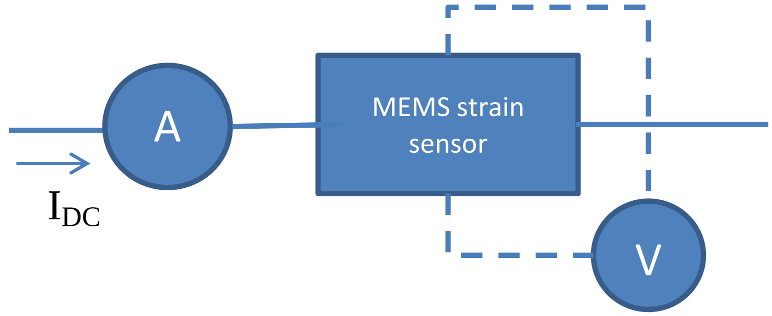

Figure 9: Electrical circuit lay-out of the set-up used in the V-I characterization of the MEMS strain sensor. In measuring the rise times and fall times, the voltmeter in the set-up is replaced by a digital oscilloscope. The sensor conditioner/voltage source is not shown.

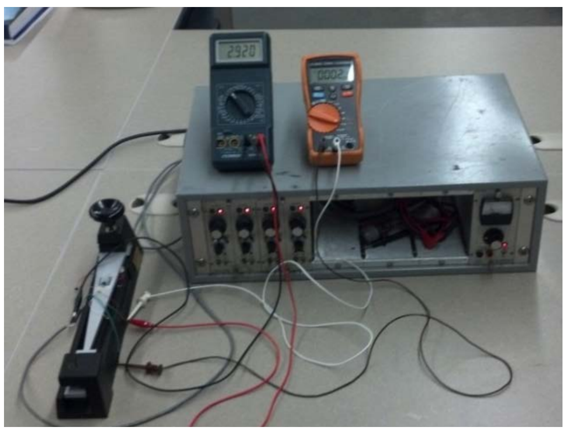

Figure 10: Experimental set-up showing the bend test module and accessories used in the V-I characterization experiments. The same set-up was utilized to carry out the characterization in high temperature and low temperature environments.

4.4 Dynamic testing method

Dynamic performance characterization was carried out using a rectangular aluminum 6061 beam. The test beam has dimensions of 0.40 m x 0.064 m x 0.0016 m. After sensor installation, the aluminum beam was assembled with one end fixed into the head of an Unholtz-Dickie 512M electrodynamic shaker table as shown in figure 11. The fixed end of the cantilever was bolted into a steel metal block assembly. Magnitude response of the cantilever beam was obtained by varying the input frequency to the shaker from 0 Hz to 220 Hz using a Krohn-Hite 5300A function generator. Measurement of the input frequency was monitored by a Hewlett-Packard 5314a universal counter. For each frequency, the voltage response and amplitude were recorded for the MEMS sensor and the strain gauge. Sensor voltage response was recorded using the TPS 2012 Tektronix digital storage scope. The storage scope's sampling frequency was set at 5 kHz and a total of 2500 data points were obtained for each run. This is equivalent to a time series with length interval of 0.5 s. Analysis focused on the three resonant frequencies observed since the amplitudes of the AC voltage output in these frequencies are uniform and well defined. Vibration data from the three resonant frequencies were post-processed for noise filtering and FFT. The filtering was implemented using a MATLAB-based low pass finite impulse response (FIR) digital filter. Comparisons were made on both raw and filtered sensor signal.

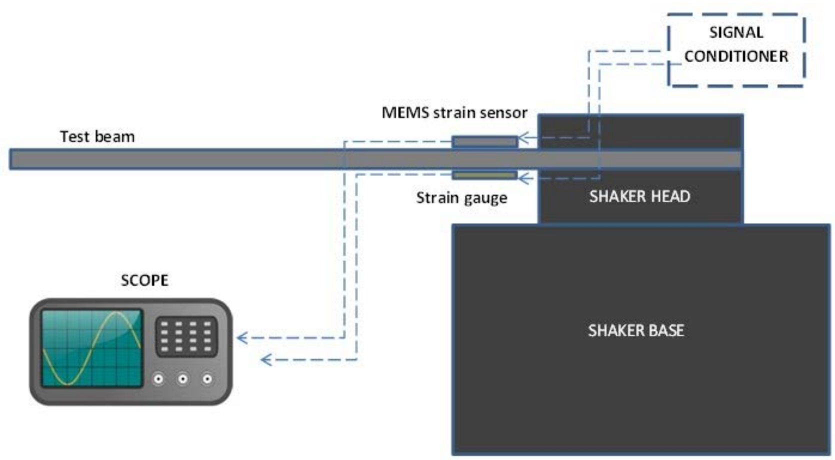

Figure 11: Schematic diagram of the dynamic test set-up using the electodynamic shaker table. The controls for the shaker table are not shown. The same set-up was utilized in the extended vibration testing of the MEMS strain sensors performed at a frequency of 175 Hz.

4.5 Extended Vibration testing of the MEMS strain sensor

Using the dynamic test set-up, extended vibration testing was done on the MEMS strain sensor using 175 Hz frequency vibration which is the test beam's third resonant frequency. The frequency used was the highest resonant frequency measured for the cantilever beam. A MEMS strain sensor was tested until failure in the sensor output voltage was observed. The storage scope was set to pulse-width trigger mode in order to capture the instant of the fault. The pulse width trigger mode was used since a sensor failure event is expected to result in a sudden drop in the voltage thereby changing the pulse width of the output AC voltage. Sensor voltage output was sampled every 1-hour interval for the whole duration of the vibration testing. The voltage time-series was converted to strain-time histories for cycle counting, using the sensor sensitivity obtained from static testing. The sensor was visually examined for any external failures i.e. failed sensor-to-metal bonding or wire leads. Rainflow cycle counting was performed using Scanimetrics Motescan v.2.38.1 software and results were compared for the filtered and unfiltered MEMS sensor output to check how noise affects fatigue lifetime estimates.

Chapter 5

RESULTS OF SENSOR PERFORMANCE CHARACTERIZATION AND DISCUSSIONS

Evaluation performed on the strain sensors determined the following sensor characteristics: (a) static strain response, (b) electrical switching properties, (c) dynamic response and (d) sensor performance under extended vibration. Results of the sensor characterization procedures and relevant discussions are presented in this section.

5.1 Static Strain Response characteristics

A sensor installed on a steel test bar was tested using direct tension method performed in a MTS machine. Results show that the MEMS sensor response to uniaxial tensile strain was linear before the onset of failure in the strain range of 0 to 2691 με. The voltage response as a function of the reference strain, shown in figure 12, shows that the MEMS sensor voltage increased uniformly with the increasing applied tensile strain. A sudden drop in the sensor voltage followed as partial failure in the sensor bonding occurred, indicated by the first peak in the graph. After the failure, the sensor output signal recovered with a smaller slope. A second failure occurred at a strain value of 5442 με as shown by the second peak in the graph, followed by a drop in the sensor voltage. At this point, sensor voltage has stopped responding to further increase in the applied strain. A best-fit line in the region before failure shows that the sensor has sensitivity of 0.065 mV/με. Sensor response from 0 to 2691 με showed good linearity as indicated by an R-square fitting value of 0.99 shown in figure 13. This result demonstrates that the sensor can perform reliably for a strain range even beyond the onset of plastic deformation at 2000 με.

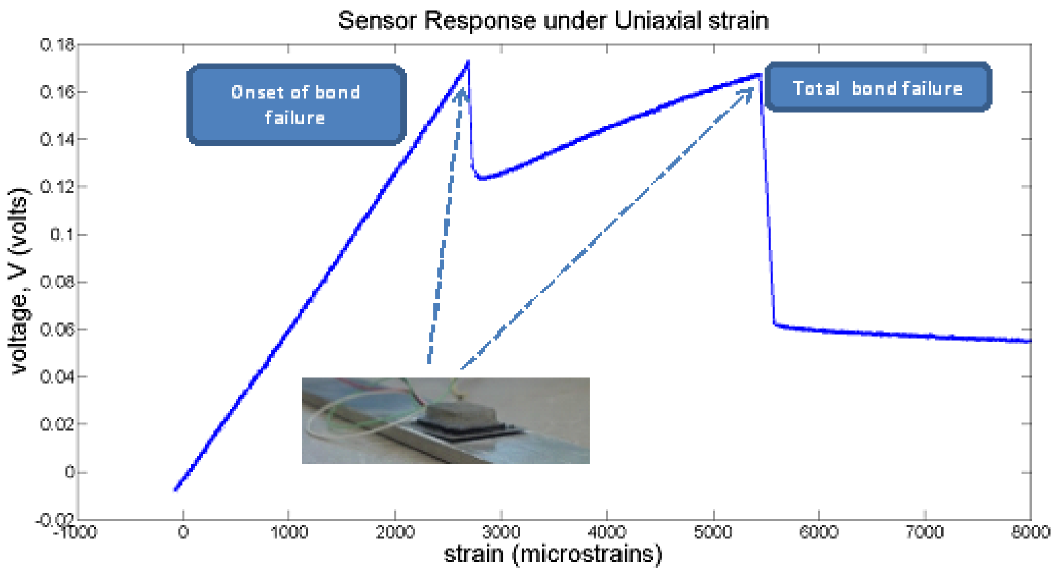

Figure 32: Voltage response of the MEMS strain sensor under direct tensile strain. Inset shows the MEMS sensor after testing, with the steel base detached from the test beam. The first peak (2691 με) shows the onset of the bond failure. The second peak (5442 με) shows the point where total bond failure occured followed by a drop in the voltage signal

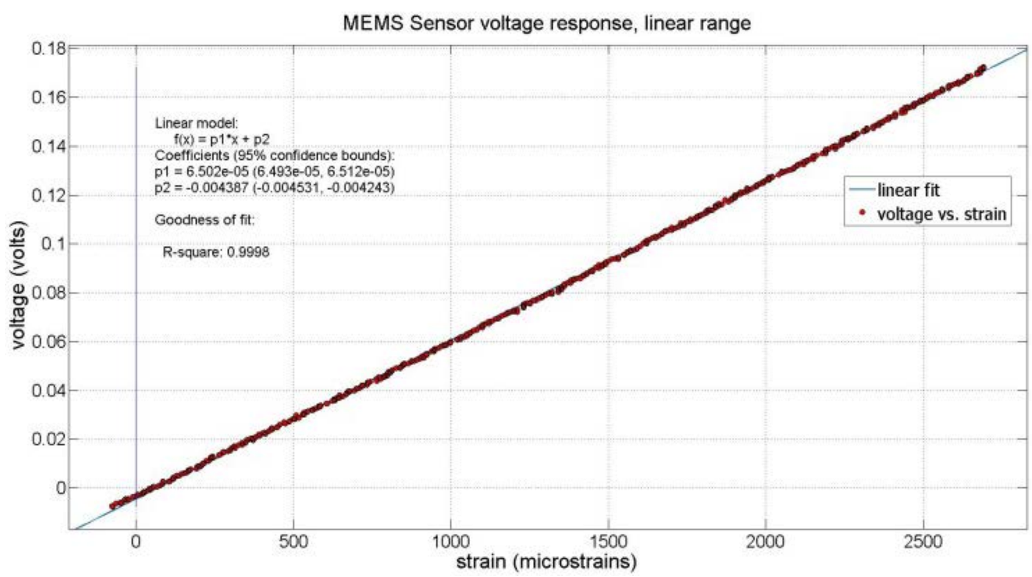

Figure 13: The range of the sensor voltage response of the MEMS sensor before the onset of failure. The observed response has good linearity as indicated by R^2 = 0.99 with a measured sensor sensitivity of 0.065 mV/με. The strain range was determined to be a from 0 to 2691 με.

The MEMS sensor response to bending tensile strain using the constant stress cantilever beam method is shown in Figure 14. The result indicates good linear response and a sensor sensitivity of 0.05 mV/με. Sensor response to bending compressive strain shown in Figure 15 closely agrees with the tensile strain result, with sensor sensitivity 0.054 mV/με. The difference could have been due to an alignment error after repositioning of the test beam during changing set-ups from tensile to compressive strain set-up. A small amount of offset voltage is also measured for both tensile and compressive strain. This observed offset is simply an artifact of the MEMS sensor fabrication process.

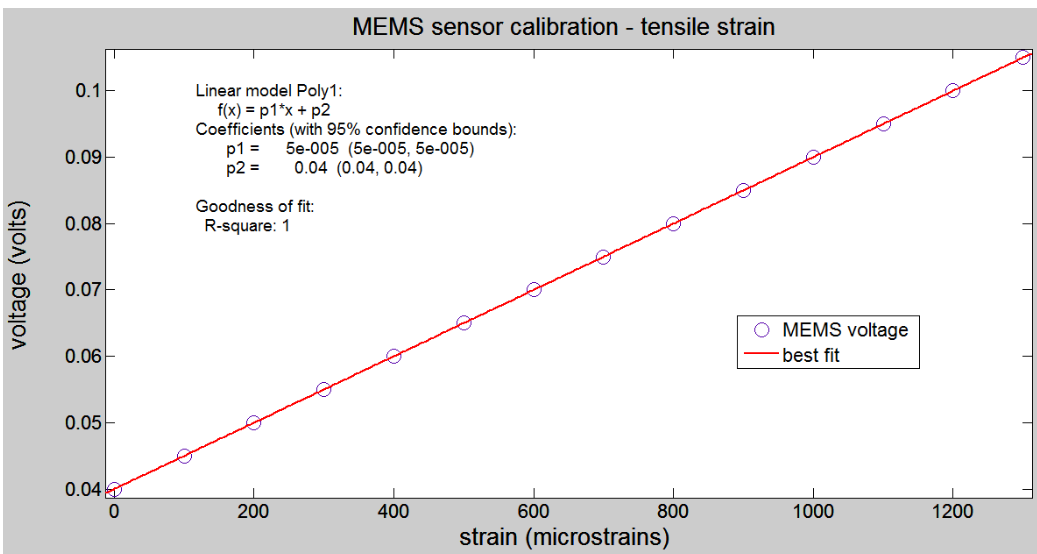

Figure 14: MEMS strain sensor response to tensile strain. The sensor sensitivity indicated by the slope of the best-fit line is measured as 0.05 mV/με. The R-square value is 1.0.

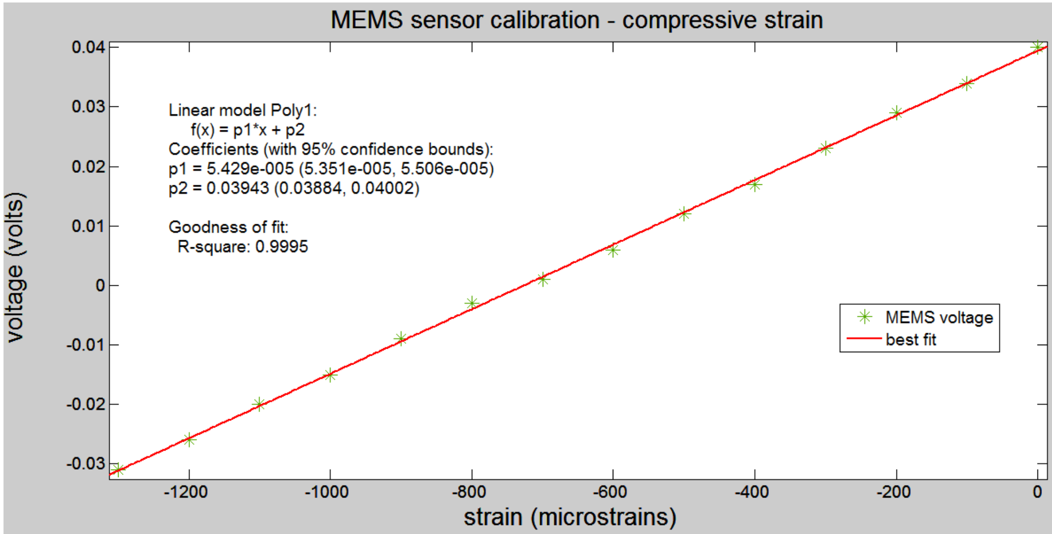

Figure 15: MEMS sensor response to compressive strain. The sensor sensitivity indicated by the slope of the best-fit line is measured as 0.054 mV/με. The R-square value is 0.99.

From the measured sensitivities, the gauge factor for each of the different calibration procedures was calculated using equation (3.6). The gauge factor values are summarized in Table 1. It was found that results for the compressive bend test and tensile bend test have minimal difference. The difference could be due to a small alignment error when changing experimental set-ups from compressive to tensile test. Direct tension test revealed a gauge factor value higher than that of the tensile and compressive bend tests. The gauge factors achieved by the MEMS strain sensor are 5 to 6 times higher than the reference foil gauge's gauge factor of 2.17. This higher gauge factor of the prototype MEMS strain sensor is an indication of better strain sensing performance.

Table 1: Summary of the measured sensitivity and calculated gauge factors obtained from different calibration procedures

Test Method	Sensitivity (mV/microstrains)	Calculated Gauge Factor
Compressive Bend test	0.0543	10.86
Tensile Bend test	0.050	10.0
Direct tension test	0.065	13.0

5.2 Electrical and switching characteristics

The electrical properties of the prototype MEMS strain sensor during switching events were determined at temperatures of 24 ^{o}C, -20 ^{o}C and 80 ^{o}C. Temperature fluctuations were limited to within ±2 ^{o}C of a set-point temperature. The MEMS sensor was bonded to a constant stress cantilever beam and measurements were obtained for the loaded and unloaded cases. In the loaded case, the MEMS sensor has a bending strain load of 221 $\mu\varepsilon$. The voltage-time profile during switch-on/switch off was determined for the loaded and unloaded cases using a digital storage oscilloscope. Voltage-current (V-I) measurements of an unloaded sensor at 24 ^{o}C shown in figure 16 show that the resistance of the device is constant and is not affected by increasing voltage. A best-fit line of the data shows that the sensor is similar to a metal-foil strain gauge, exhibiting ohmic characteristic with a resistance of 1250 Ω.

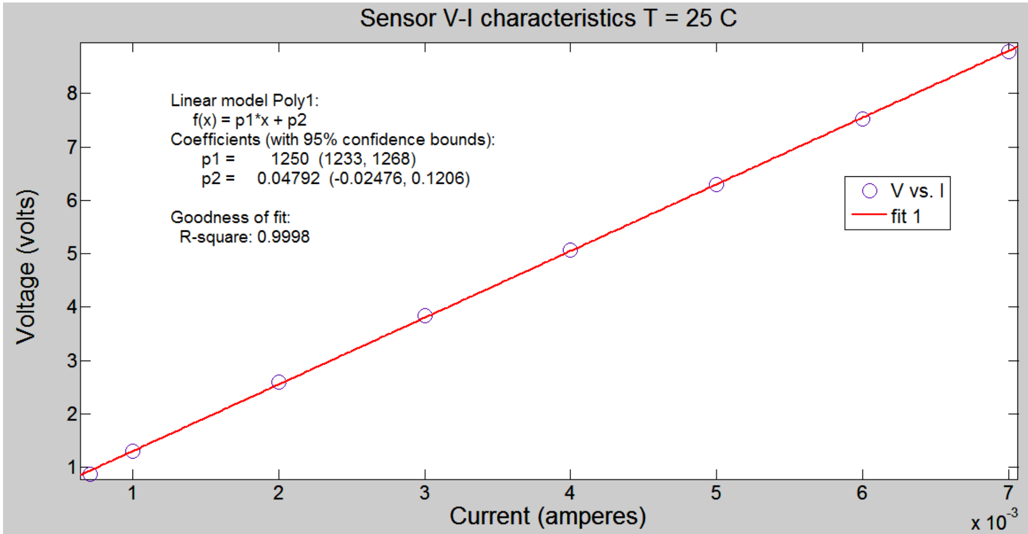

Figure 16: V-I graph of an unloaded MEMS strain sensor at 24 °C. Linear change of current with current was observed (R^2 = 0.99) indicating good ohmic behavior. Sensor resistance was measured to be 1250 ohms.

The voltage step-response of the prototype MEMS strain sensor showing the voltage rise/drop during switching events were obtained to measure the sensor's voltage rise times and fall times. A summary of sample voltage-time profiles obtained at room temperature (24 °C) is shown in Table 2. The rise time is the time it took the voltage to go from 0 to 90% of the maximum voltage during a swich-on event. On the other hand, the fall time is the time it took the voltage to go from 100% to 10% of the maximum voltage during a switch off event. Figures (a) and (b) of Table 1 shows the switch-on and switch-off events of the MEMS strain sensor when there is no load on the test beam. Figures (c) and (d) shows the switch-on and swtich-off events of the MEMS strain sensor when there is a strain of 221 με in the beam.

Table 2: Summary of the voltage-time responses of the MEMS strain sensor during switch-on and switch off events obtained at T = 24 C. Switch-on and switch-off are shown by the voltage step response. Figures (a) and (b) refers to the switch-on and switch-off events from an unstrained beam. Figures (c) and (d) shows the switch-on and switch-off events for a strained beam

<table>
<tr><th>Case</th><th>Switch-on</th><th>Switch-off</th></tr>
<tr><td>Unloaded</td><td>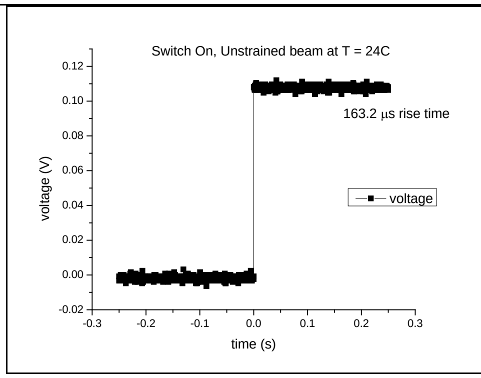

(a)</td><td>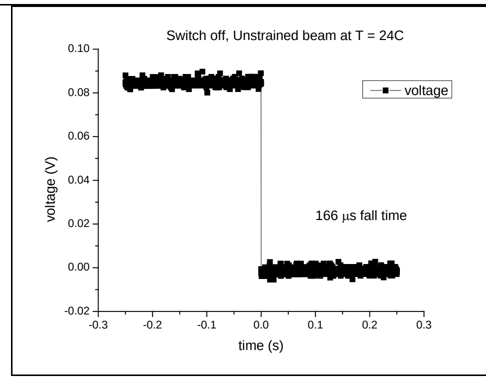

(b)</td></tr>
<tr><td>Loaded</td><td>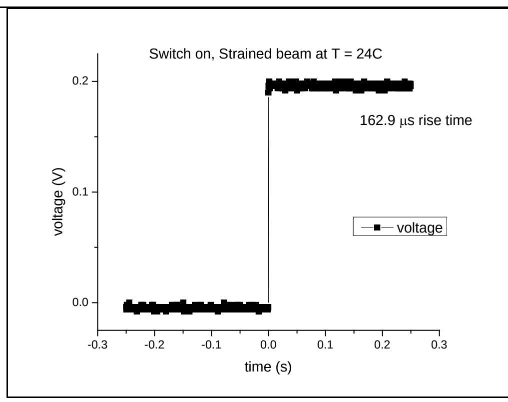

(c)</td><td>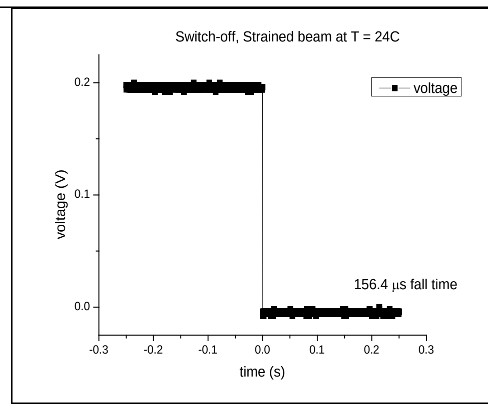

(d)</td></tr>
</table>

A summary of the voltage rise times and fall times, obtained over the temperatures of 24 ^{o}C, -20 ^{o}C and 80 ^{o}C is shown in Table 3. The rise times and fall times reported were averaged over thirty measurements. At similar temperatures, it was observed that the average rise/fall times does not change significantly with the application of strain. This suggests that the applied strain doesn't affect the measured rise/fall times.

On the other hand, comparing measurements obtained at different temperatures, the average rise/fall times measured at 24 ^{o}C and 80 ^{o}C were found to have a small difference. Further inspection of the data revealed that this difference is not significant as shown by the standard deviations. The calculated standard deviations indicate that the range of rise/fall times measured at 24 ^{o}C is well within the range of expected rise/fall times for 80 ^{o}C. It was found as well that the average rise/fall times obtained at -20 ^{o}C was significantly lowered. The reduction is about 50% of the average rise/fall time values obtained for 24 ^{o}C and 80 ^{o}C. These results suggest that the sensor rise and fall times increase with temperature and reaches a saturation at room temperature as indicated by the minimal change in the average rise/fall times between 24 ^{o}C and 80 ^{o}C. This could further indicate that the voltage step-response at 24 ^{o}C and 80 ^{o}C is the same. The variability of the measured rise/fall times was observed to increase at 80 ^{o}C. This could be a manifestation of increased interference of thermal noise in the sensor performance at elevated temperatures. Reduced rise/fall times at -20 ^{o}C indicate a faster sensor response time to input voltage at low temperature. The improved voltage settling time is a desirable characteristic for sensors relying on battery power e.g. short fall times result to longer battery life. This improved voltage response at -20 ^{o}C can also suggest that the rise/fall times can further decrease at much lower temperatures and will result to even faster sensor voltage response.

Table 3: Sensor response time and average power at switch-on obtained at different temperatures for the loaded and unloaded beam cases. Measurements were repeated 30 times to obtain the reported average and standard deviation.

Temperature	Case	Rise time, μs	Fall time, μs	Steady-state power, μW
-20^{o}C	Unloaded	83.01 ± 3.41	82.15 ± 3.00	287.0 ± 6.4
	Loaded	83.68 ± 2.79	83.85 ± 2.97	783.6 ± 2.4
24^{o}C	Unloaded	164.3 ± 4.2	163.3 ± 3.8	267.6 ± 0.5
	Loaded	162.6 ± 4.0	160.3 ± 2.8	494.3 ± 0.6
80^{o}C	Unloaded	166.7 ± 11.7	161.5 ± 7.3	212.7 ± 1.1
	Loaded	167.2 ± 10.0	162.1 ± 4.7	423.2 ± 7.0

*Figures reported were averaged over 30 measurements to obtain the variability. Strain used for the loaded case is 221 microstrains equivalent to a beam deflection of 15.00 mm

A strong effect of loading was observed on the power consumption of the MEMS sensor. Increased steady-state power for all loaded cases was demonstrated in all temperatures tested. Moreover, highest average power was measured at -20 ^{o}C while lowest average power was observed at 80 ^{o}C. The increased power suggests that the sensor resistance has decreased with temperature, indicating that the electrical behavior of the sensor is now similar to a metallic conductor. These findings further suggest that increased average power consumption of the prototype MEMS strain sensor is expected at even lower temperatures.

5.3 Sensor dynamic response characteristics

A prototype MEMS sensor, together with a reference strain gauge were installed in a rectangular aluminum cantilever beam and subjected to vibration testing using an electrodynamic shaker table. A frequency sweep from 0 Hz to 220 Hz was used to identify the test beam's resonant frequencies. The AC voltage outputs from the MEMS sensor and the strain gauge were monitored by a digital storage oscilloscope to determine the signal amplitude and obtain a snapshot of the time series. Characterization of the beam vibration was carried out by measuring the amplitude response of the foil strain gauge across the frequencies swept, as shown in figure 17. The three resonant frequencies of the cantilever beam, indicated by the peaks, were determined to be as 10 Hz, 63 Hz and 175 Hz. Reduced beam vibrations at frequencies far from the resonant frequencies resulted in low voltage amplitudes, suggesting that the sensor dynamic response is best to be investigated at the beam's resonant frequencies. The strain amplitudes in these peaks were determined to be 706 microstrains for 10 Hz; 659 microstrains for 63 Hz; and 588 microstrains for 175 Hz vibration. These strain values are all within the aluminum beam's elastic limit.

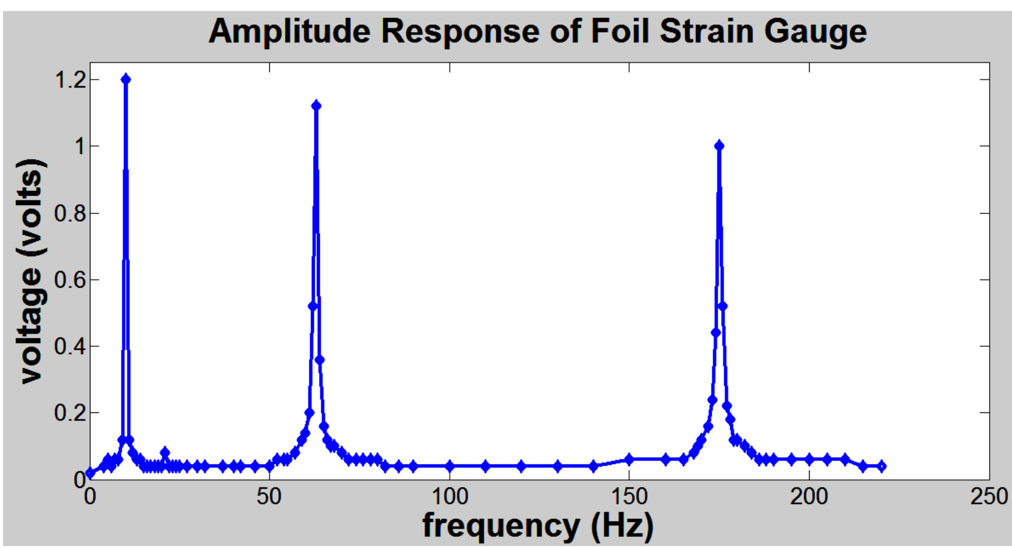

Figure 17: The amplitude response of the aluminum test beam, as picked up by the foil strain gauge. The three peaks are the resonant natural frequencies of the rectangular aluminum test beam. The resonant peaks are centered at 10 Hz, 63 Hz and 175 Hz.

Figure 18 shows the time series and the frequency spectrum of the MEMS sensor voltage response obtained at 10 Hz, 63 Hz and 175 Hz. The initial raw data was detrended to remove bias from the conditioning circuit. The presence of noise was observed for all of the time series. The noise, which manifested as small spikes along the length of the sinusoid, appears to be a high frequency noise. Performing a discrete Fourier transform on the time series however reveals only a single peak indicating that there is only a single frequency component in the vibration. The 10-Hz vibration data revealed a response of 9.77 Hz, while the time series for the 63-Hz vibration has a response at 62.3 Hz. Lastly, the 175-Hz vibration has a response at 175.17 Hz.

In contrast, the strain gauge's voltage signal was observed to have minimal amount of noise unlike in the MEMS strain sensor voltage's signal as shown in Figure 19. The AC voltage output is a regular sinusoid. Discrete Fourier transform of each time series revealed a single peak with a frequency exactly similar with those obtained from the MEMS sensor discrete Fourier transform. This result strongly suggests that the response of the prototype MEMS strain sensor and the standard strain gauge are identical at the excitation frequencies tested.

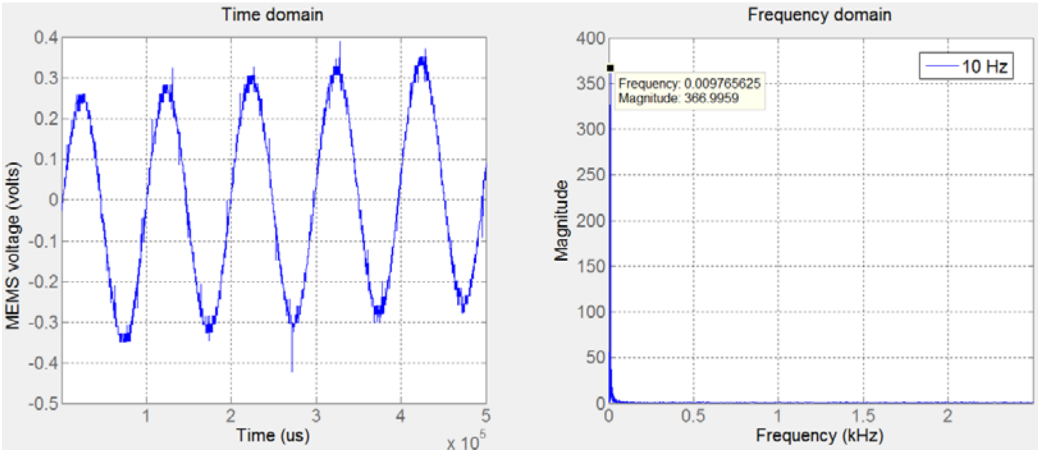

(a)

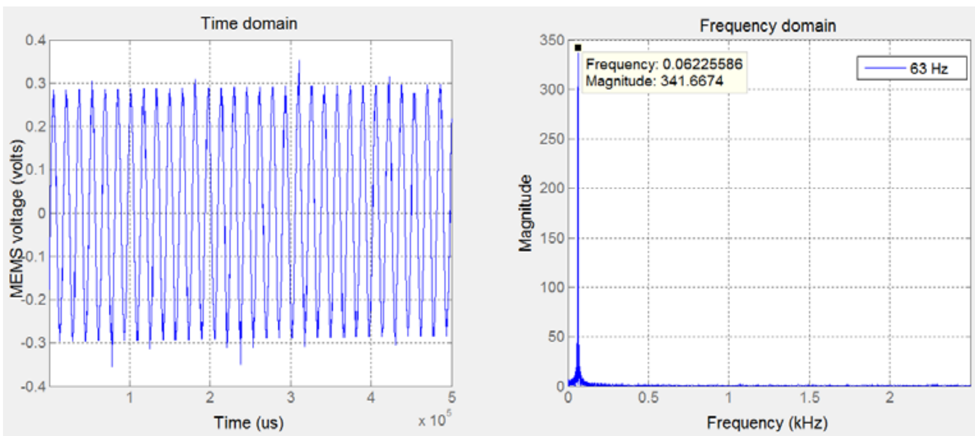

(b)

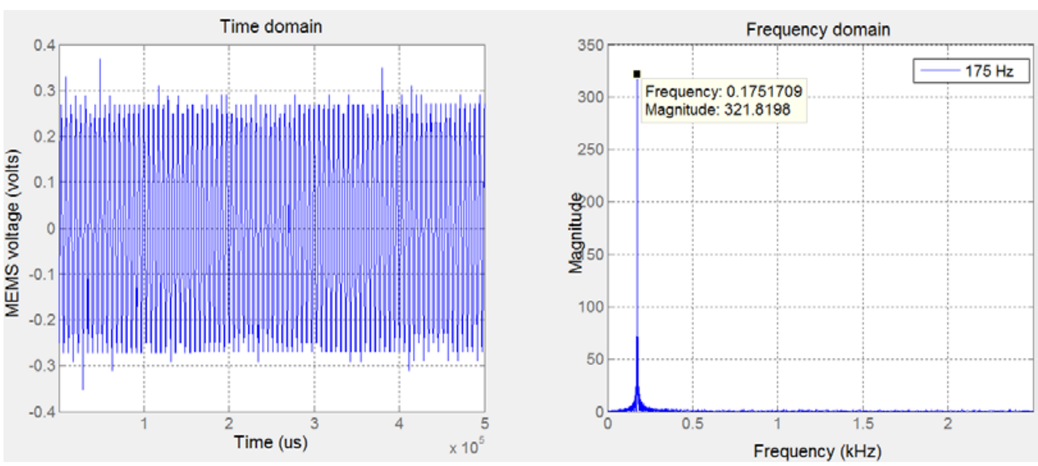

(c)

Figure 18: Time and frequency domain representation of the MEMS sensor voltage response at (a) 10 Hz (b) 63 Hz and (c) 175 Hz. MEMS voltage output clearly shows the presence of noise. Response of the sensor reveals frequency peaks at 9.77 Hz, 62.3 Hz and 175.17 Hz, close to their respective input frequencies.

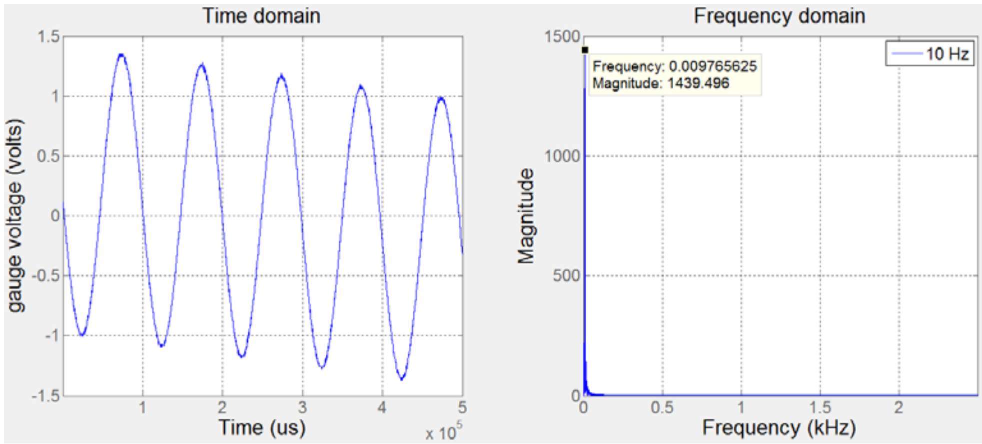

(a)

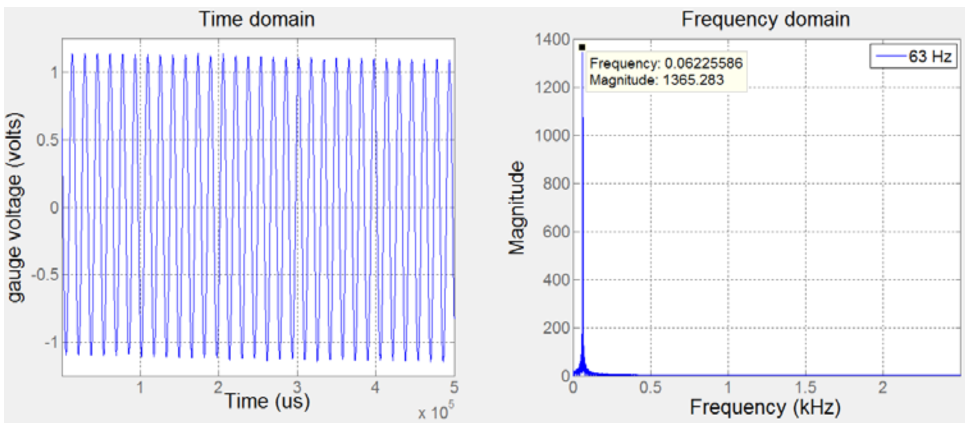

(b)

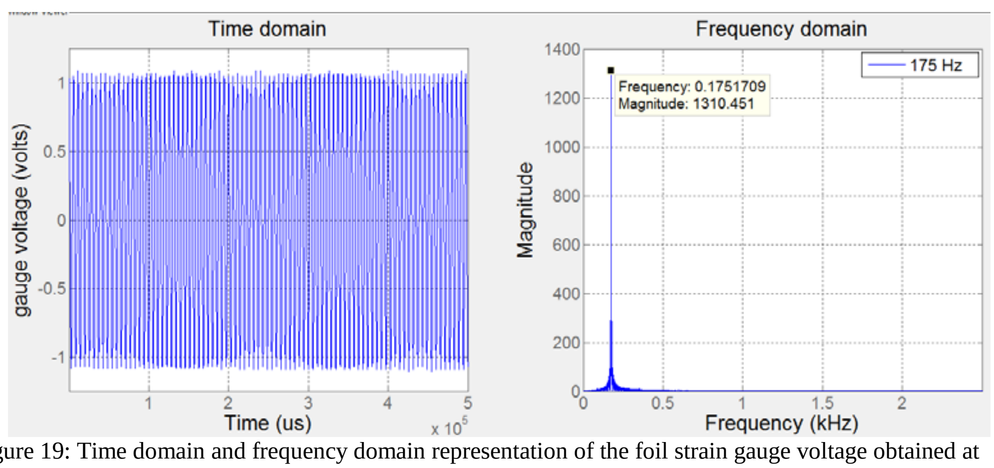

Figure 19: Time domain and frequency domain representation of the foil strain gauge voltage obtained at vibration frequency of (a) 10 Hz, (b) 63 Hz and (c) 175 Hz. Discrete Fourier transforms of each time series revealed that the MEMS and strain gauge were able to recover the same frequency peaks. This indicates that the prototype MEMS strain sensor and the metal-foil strain gauge have the same response at the frequencies tested.

Another way of visualizing the noise in the MEMS voltage signal is by plotting the MEMS voltage response against the reference strain. Ideally, the data points should be contained within a straight line. Actual data points from 10 Hz, 63 Hz and 175 Hz vibration data however consolidated into a band in the scatter plot as shown in Figure 20. This indicates the presence of noise. Using a linear regression fit to describe the scatter plots, the slope of the best-fit lines obtained closely agree with each other, indicating a sensor sensitivity of ~0.42 mV/$\mu\varepsilon$.

To probe the nature of the noise observed in the time series, the residuals of the data points were analyzed. The residual values, plotted as a histogram shown in Figure 21, were observed to assume a nearly-Gaussian distribution in all frequencies tested. A Gaussian fitting function indicated by the red curve in the graph further emphasizes this observation. This characteristic of the residuals distribution shows that the noise involved in the measurements is approximately white noise and is similar for all three vibration data.

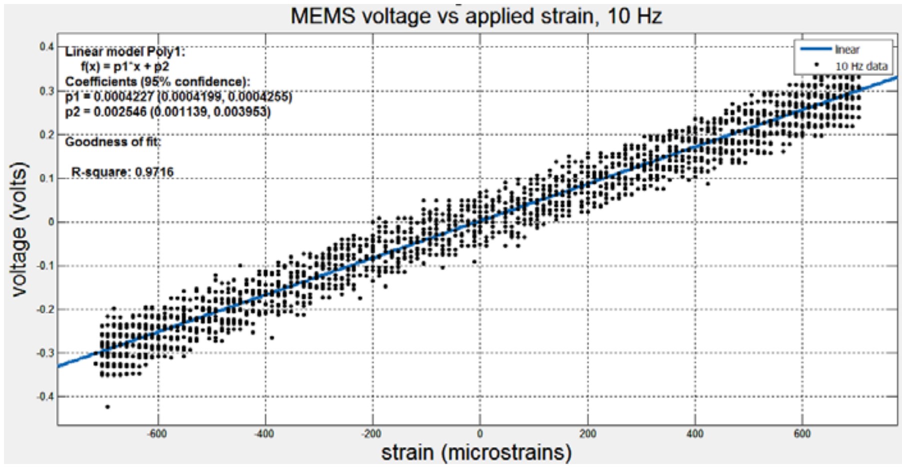

(a)

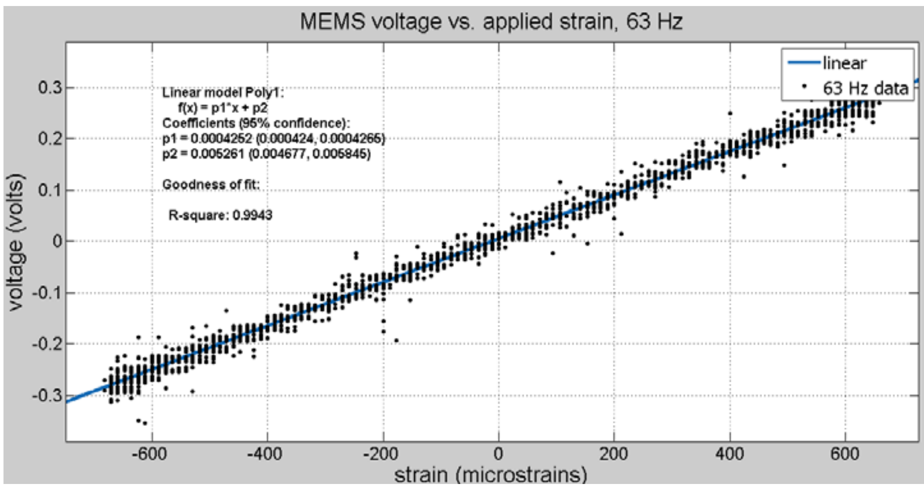

(b)

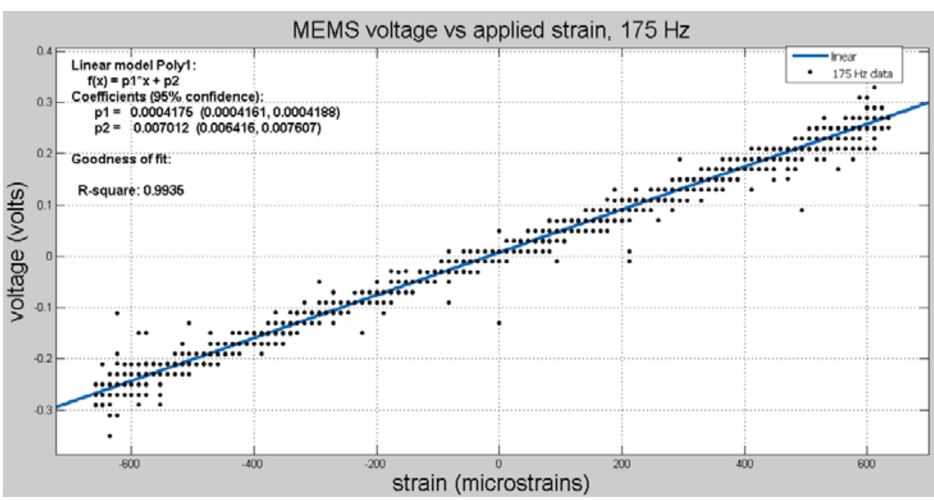

(c)

Figure 20: Plot of the MEMS sensor dynamic voltage vs. reference strain obtained at (a) 10 Hz, (b) 63 Hz and (c)175 Hz. Best-fit line indicate a sensor sensitivity of 0.42 mV/με

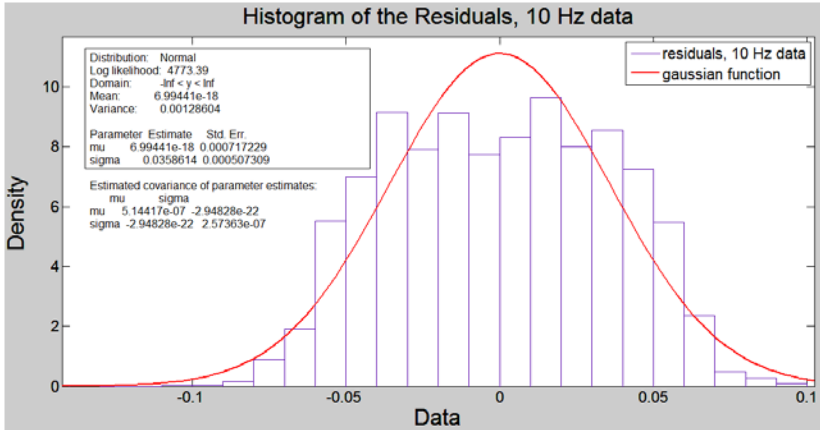

(a)

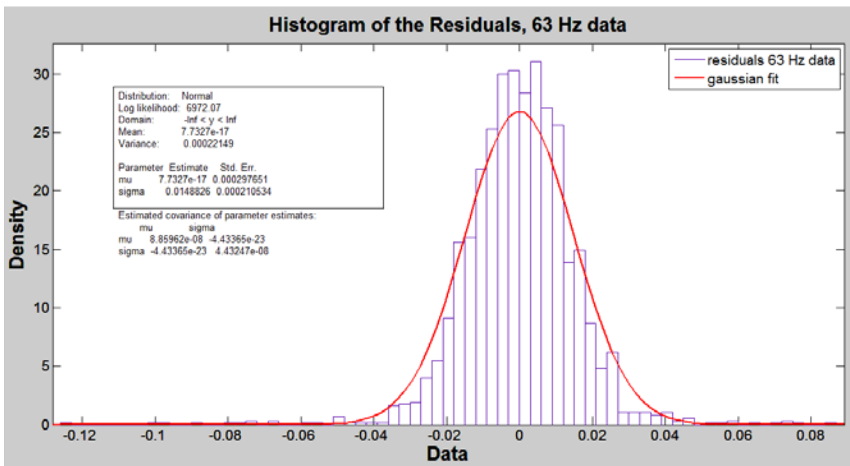

(b)

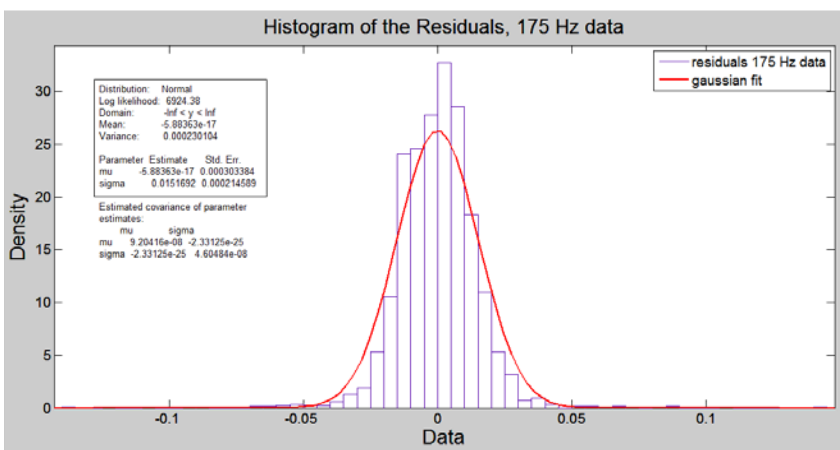

(c)

Figure 21: Residuals histogram plot for the (a) 10 Hz (b) 63 Hz and (c)175 Hz vibration data. Results show that the noise has a distribution similar to a Guassian fitting function (red line) indicating that the noise is approximately white noise

A low-pass Butterworth-type equiripple finite impulse response (FIR) filter was designed and implemented in MATLAB for post processing of signal from the MEMS strain sensors. The filter was designed to pass all frequencies below 200 Hz and completely attenuate any component above 250 Hz as shown in Figure 22. As shown in Figure 23, filtering process of a noisy 175-Hz vibration data improves the output signal. It however introduces a phase shift in the filtered signal but retains the same frequency as indicated by the frequency peak in the signal's Fourier transform.

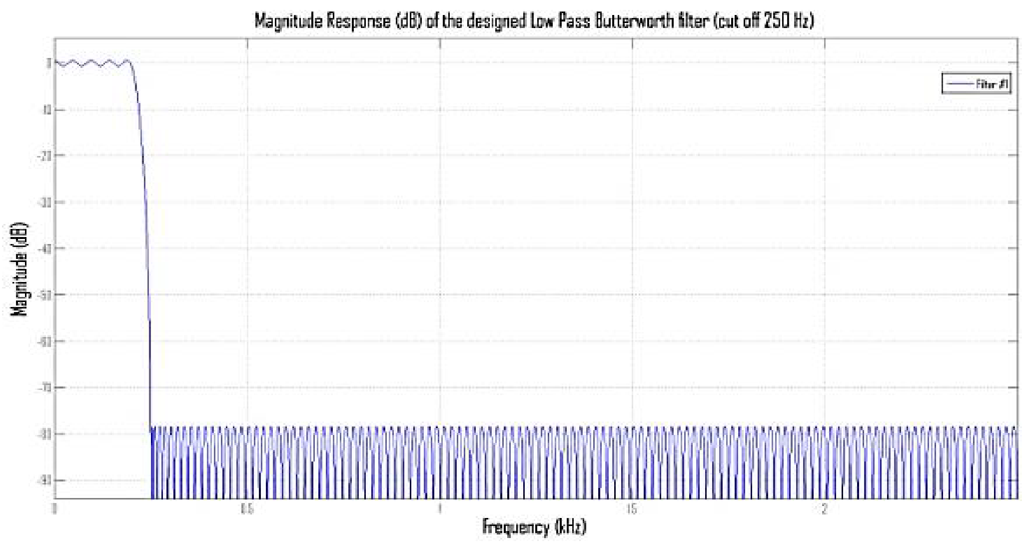

Figure 22: Magnitude response of the low pass FIR filter designed for noise filtering of the MEMS strain sensor signals. The cut-off frequency is at 200 Hz.

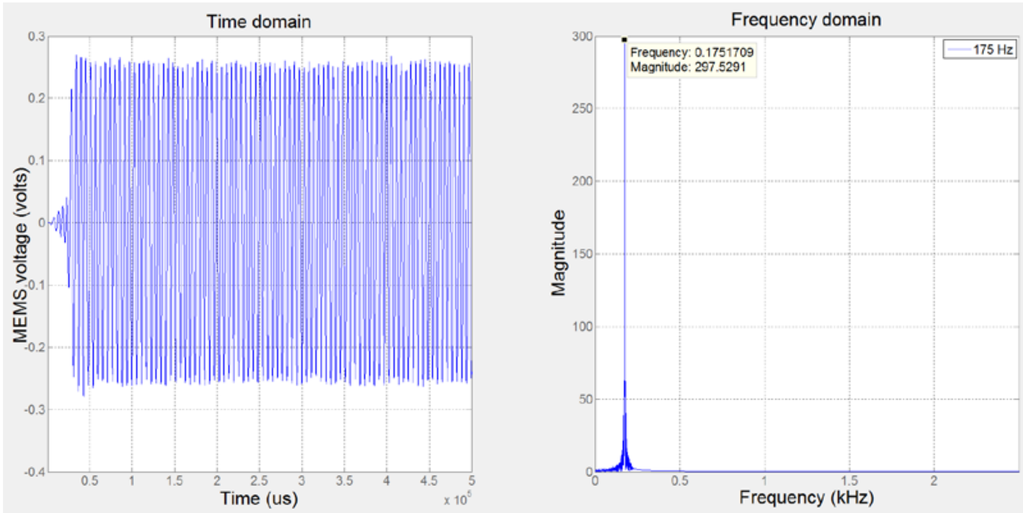

Figure 23: Time series and frequency spectrum of the filtered 175-Hz MEMS sensor signal. The noise filtering introduces a phase shift manifested as a delay in the voltage response. The response of the filtered and unfiltered signal is identical.

5.4 Sensor performance and reliability under extended vibration

After investigating the sensor dynamic response, the MEMS strain sensor performance was tested under extended vibration at 175 Hz. Results of the extended vibration testing on the MEMS strain sensor showed that the prototype MEMS sensor can endure extended duration of vibrations. Though failure in the sensor voltage output occurred after logging an aggregate of 260 minutes, the cause of the failure is due only to detached lead wires. It was noted that both the sensor's device chip and its bonding were intact.

Comparison between the MEMS sensor's filtered and unfiltered strain histories were made using the strain gauge's time series as reference. Using a strain history with time length of 0.50 s, the number of loading cycles and the equivalent strain range were calculated by rainflow counting method. Results of rainflow cycle counting are presented in Table 4.

Table 4: Cycle counts calculated using rainflow counting of the MEMS and strain gauge strain history. The time series has a length of 0.50 seconds

Time series	Number of cycles (t = 0.50 s)	Number of cycles (t = 260 min)	Equivalent strain (microstrains)
strain gauge (reference)	87	2.71×10^6	1261.76
Unfiltered MEMS	100	3.12×10^6	1273.18
Filtered MEMS	86.5	2.69×10^6	1203.94

From the short strain history, results show that the cycle counts for the strain gauge (87 cycles) and the filtered MEMS signal (86.5 cycles) closely agree with each other. The unfiltered MEMS signal revealed 100 cycles which is higher than those obtained from the filtered MEMS and strain gauge signal. The difference appears to be small but in the extended vibration test of 260 minutes, the unfiltered MEMS signal reveals 3.12 million cycles. This figure is significantly larger than 2.69 million cycles for the filtered MEMS and 2.7 million cycles for the strain gauge signal. The higher cycle count in the unfiltered MEMS signal shows that the noise in the signal causes the overestimation of the loading cycles in the rainflow counting.

Strain range calculations showed an equivalent strain of 1273 $\mu\varepsilon$ obtained from the unfiltered MEMS signal. This figure is larger than the 1262 $\mu\varepsilon$ equivalent strain obtained from the reference strain gauge. However, the filtered MEMS signal only has an equivalent strain of 1204 $\mu\varepsilon$ which is remarkably lower than the value from the strain gauge. Comparing the two equivalent strain values obtained from the MEMS sensor, the unfiltered MEMS signal's equivalent strain has better agreement with the strain gauge's equivalent strain. This result clearly shows that the process of filtering noise leads to underestimation of the equivalent strain. A consequence of this result is that the strain history coming from the filtered MEMS signal will give a conservative fatigue life estimate of the test specimen.

The effect of the noise in the unfiltered MEMS signal results to overestimation of the fatigue life as it returns a higher equivalent strain value and high number of cycles. Noise filtering of the sensor output signal on the other hand result to a conservative estimate of the fatigue damage as it leads to underestimated strain range. Nonetheless, the extended vibration testing was able to show that the prototype MEMS strain sensor's fatigue lifetime is more than 2.7 million cycles at an equivalent strain range within the elastic limit. It can be noted also that the sensor bonding on the test specimen didn't contribute to the failure and the sensor's device chip is completely intact.

Chapter 6

SUMMARY OF CONCLUSIONS AND RECOMMENDATIONS FOR FUTURE WORK

Static bending calibration, electrical characterization, dynamic testing and extended vibration testing were carried out on a prototype piezoresistive silicon MEMS strain sensor to evaluate performance and reliability. The ASTM E-251-92 standard for testing metallic bonded resistance strain gauges was adapted for the testing and calibration procedures.

Uniaxial direct strain testing results revealed that the MEMS strain sensor was able to maintain linear response for a strain range of 0 to 2691 $\mu\varepsilon$ before failure. The sensor also achieved a strain sensitivity of 0.065 mV/$\mu\varepsilon$ and a gauge factor value of 13.0. Sensitivity obtained from compressive and tensile bending was found to be 0.0543 and 0.05 mV/$\mu\varepsilon$, which clearly agrees with each other. The corresponding gauge factors were calculated to be 10.86 for compressive bending and 10.0 for tensile bending. These static calibration results have demonstrated good linear response to input strain and significantly higher gauge factor compared to the foil gauge.

Electrical V-I characterization revealed good ohmic behavior. It was observed that voltage rise time and fall time is fastest when the sensor is operating at -20^{o}C. Moreover, there was no significant difference in the voltage rise times and fall times for sensors operating at 24^{o}C and 80^{o}C. Average power consumption of the sensor was observed to be higher for the loaded case compared to the unloaded case for all temperatures tested due to increased sensor resistance in the loaded case. Average power consumption of the sensor was observed to decrease with increasing operating temperature. This is an indication that the sensor resistance increases with temperature and the sensor electrical behavior is similar to a metallic conductor.

Dynamic testing results at 10 Hz, 63 Hz and 175 Hz showed that the MEMS strain sensor contained noise in its voltage signal output. In contrast, the reference foil strain gauge output has minimal to almost zero noise. The noise in the signal appeared to increase with the frequency of vibration. This observation shows the need for a filter to clean the sensor output signal. However, performing a Fourier transform on the unfiltered voltage output time series revealed that the response of the MEMS strain sensor and the reference foil gauge is identical for all frequencies tested. A digital low pass Butterworth FIR filter was used to filter the noise from the MEMS raw signal.

Extended vibration tests at 175 Hz showed that the MEMS strain sensor was able to operate for an aggregate of 260 minutes before failure. Inspection of the sensor revealed failure in the wire leads and not on the device chip while the bonding of the sensor to the test specimen has remained intact. Rainflow counting method was performed using Scanimetrics Motescan software to determine the number of loading cycles in the filtered and unfiltered MEMS sensor signal, as well as in the foil gauge's signal. It was found that the noise in the unfiltered MEMS signal contributed to over-counting of the cycles. On the other hand, the calculated equivalent strain from the filtered MEMS signal was lower than that obtained from the reference suggesting that the fatigue lifetime estimate from this signal is conservative. The device lifetime before failure was measured to be 2.7 million cycles. Considering that the failure observed is due only to detached wires, therefore the prototype MEMS strain sensor has a lifetime of more than 2.7 million cycles.

While most of the characteristics and properties of the prototype silicon MEMS strain sensor were evaluated in this thesis, more detailed studies are needed to complete the analysis of its performance. Thus, the following recommendations are given:

(1) To understand the sensor performance at higher frequencies, dynamic testing beyond 175 Hz can be done. The prototype MEMS strain sensor has been found to perform satisfactorily at 175 Hz. Extending the tests beyond 175 Hz will be able to reveal the sensor's upper frequency limit thereby giving the full range of frequency at which this prototype sensor can be used.

(2) Repeating the sensor dynamic testing in high and low temperatures will be able to show the MEMS sensor performance under combined dynamic

mechanical and thermal loading. Combined extremes of high frequency vibration and high or low temperature will be able to characterize the limits of the sensor's applicable range of performance.

(3) Sensor response at low temperature showed shortened rise times indicating fast sensor settling time with input voltage. Measurement of sensor switching response at temperatures lower than -20^{o}C may be done to reveal much better response times or a saturation point where further decrease in temperature doesn't result to faster rise times.

(4) Vibration testing using white noise excitation can be performed as extension of the dynamic testing. This may reveal further information on fatigue lifetime measurement capability of the sensor since most fatigue measurements are performed using random vibration excitations.

BIBLIOGRAPHY

[1] V. Kliman, “Fatigue Life Prediction for a Material under programmable loading using the cyclic stress-strain properties” *Mater. Sci. Eng.* no. 68, 1-10, 1984

[2] P. K. Stein. A brief history of bonded resistance strain gages from conception to commercialization. *Exp Tech 14(5),* pp. 13-19. 1990.

[3] P. K. Stein. Strain gage history and the end of the twentieth century. *Exp Tech 25(2),* pp. 15-16. 2001.

[4] S. Huang and A. Khan. On the use of electrical-resistance metallic foil strain gages for measuring large dynamic plastic deformation. *Exp. Mech. 31(2),* pp. 122-125. 1991.

[5] K. Oi. Transient response of bonded strain gages. *Exp. Mech. 6(9),* pp. 463-469. 1966.

[6] A. J. Landgrebe. *An Analytical and Experimental Investigation of Helicopter Rotor Hover Performance and Wake Geometry Characteristics.* United Aircraft Corp. Res. Lab. East Hartford, CT, USAAMRDL Tech. Rep. 71-24, 1971.

[7] H. Choi, S. Choi and H. Cha. Structural health monitoring system based on strain gauge enabled wireless sensor nodes. Presented at Networked Sensing Systems, 2008. INSS 2008. 5th International Conference on. 2008.

[8] S. I. Kozlovskiy and I. I. Boiko. First-order piezoresistance coefficients in silicon crystals. *Sensors and Actuators A: Physical 118(1),* pp. 33-43. 2005. . DOI: http://dx.doi.org.login.ezproxy.library.ualberta.ca/10.1016/j.sna.2004.07.003.

[9] Y. Kanda. A graphical representation of the piezoresistance coefficients in silicon. *IEEE Trans. Electron Devices 29(1),* pp. 64-70. 1982.

[10] Y. Kanda. Piezoresistance effect of silicon. *Sensors and Actuators A: Physical 28(2),* pp. 83-91. 1991. . DOI: http://dx.doi.org.login.ezproxy.library.ualberta.ca/10.1016/0924-4247(91)85017-I.

[11] P. French and A. Evans. Polysilicon strain sensors using shear piezoresistance. *Sensors and Actuators 15(3),* pp. 257-272. 1988.

[12] D. Schubert, W. Jenschke, T. Uhlig and F. Schmidt. Piezoresistive properties of polycrystalline and crystalline silicon films. *Sensors and Actuators 11(2),* pp. 145-155. 1987.

[13] K. E. Petersen. Silicon as a mechanical material. *Proc IEEE 70(5),* pp. 420-457. 1982.

[14] A. A. Barlian, W. Park, J. R. Mallon, A. J. Rastegar and B. L. Pruitt. Review: Semiconductor piezoresistance for microsystems. *Proc IEEE 97(3),* pp. 513-552. 2009.

[15] N. Yazdi, F. Ayazi and K. Najafi. Micromachined inertial sensors. *Proc IEEE 86(8),* pp. 1640-1659. 1998.

[16] F. Goericke, J. Lee and W. P. King. Microcantilever hotplates with temperature-compensated piezoresistive strain sensors. *Sensors and Actuators A: Physical 143(2),* pp. 181-190. 2008.

[17] M. Esashi, S. Sugiyama, K. Ikeda, Y. Wang and H. Miyashita. Vacuum-sealed silicon micromachined pressure sensors. *Proc IEEE 86(8),* pp. 1627-1639. 1998.

[18] Stepanova, Maria G., and Steven Dew, eds. Nanofabrication. Springer, 2012.

[19] G. T. Kovacs, N. I. Maluf and K. E. Petersen. Bulk micromachining of silicon. *Proc IEEE 86(8),* pp. 1536-1551. 1998.

[20] Gardner, Julian W., and Vijay K. Varadan. *Microsensors, MEMS and smart devices*. John Wiley & Sons, Inc., 2001.

[21] G. Higson. Recent advances in strain gauges. *J. Sci. Instrum. 41(7),* pp. 405. 1964.

[22] *Kulite Strain Gage Manual* (2011), Kulite Semiconductor Products Inc., Leonia, NJ [Online] Available: http://www.kulite.com/docs/products_overview/StrainGageManualDigital-01262012.pdf

[23] H. Kuo and W. H. Ko. Smart-cut™ piezoresistive strain sensors for high temperature applications. Presented at Sensors, 2009 IEEE. 2009.

[24] A. Mian, J. C. Suhling and R. C. Jaeger. The van der pauw stress sensor. *Sensors Journal, IEEE 6(2),* pp. 340-356. 2006.

[25] A. A. Mohammed, W. A. Moussa and E. Lou. Optimization of geometric characteristics to improve sensing performance of MEMS piezoresistive strain sensors. *J Micromech Microengineering 20(1),* pp. 015015. 2010.

[26] A. A. Mohammed, W. A. Moussa and E. Lou. High sensitivity MEMS strain sensor: Design and simulation. *Sensors 8(4),* pp. 2642-2661. 2008.

[27] J. C. Suhling and R. C. Jaeger. Silicon piezoresistive stress sensors and their application in electronic packaging. *IEEE Sensors Journal 1(1),* pp. 14-30. 2001.

[28] M. Suster, J. Guo, N. Chaimanonart, W. H. Ko and D. J. Young. A high-performance MEMS capacitive strain sensing system. *Microelectromechanical Systems, Journal of 15(5),* pp. 1069-1077. 2006.

[29] T. Toriyama, Y. Tanimoto and S. Sugiyama. Single crystal silicon nano-wire piezoresistors for mechanical sensors. *Microelectromechanical Systems, Journal of 11(5),* pp. 605-611. 2002.

[30] C. S. Smith. Piezoresistance effect in germanium and silicon. *Physical Review 94(1),* pp. 42. 1954.

[31] J. Greenwood. Silicon in mechanical sensors. *Journal of Physics E: Scientific Instruments 21(12),* pp. 1114. 1988.

[32] J. M. Bustillo, R. T. Howe and R. S. Muller. Surface micromachining for microelectromechanical systems. *Proc IEEE 86(8),* pp. 1552-1574. 1998.

[33] L. Zhou, S. Jung, E. Brandon and T. N. Jackson. Flexible substrate micro-crystalline silicon and gated amorphous silicon strain sensors. *Electron Devices, IEEE Transactions on 53(2),* pp. 380-385. 2006.

[34] J. Parkins. Calibration and instrumentation of semiconductor strain gauges. *Strain 4(2),* pp. 10-18. 1968.

[35] Mason WP, Thurston RN. Use of piezoresistive materials in the measurement of displacement, force,and torque. J Acous Soc of Am 29:1096–1101. 1957.

[36] American Society for Testing and Materials. Philadelphia. Standard test methods for performance characteristics of metallic bonded resistance strain gages. ASTM E-251. 1992.

[37] C. Gouldstone, J. Brogan, R. Greenlaw, R. J. Gambino, J. Gutleber, S. Sampath and J. Longtin. Embedded resistive strain sensors for harsh environments. Presented at Aerospace Conference, 2006 IEEE. 2006

[38] B. Donohoe, D. Geraghty and G. E. O'Donnell. Wireless calibration of a surface acoustic wave resonator as a strain sensor. *Sensors Journal, IEEE 11(4),* pp. 1026-1032. 2011.

[39] L. Cao, T. S. Kim, J. Zhou, S. C. Mantell and D. L. Polla. Calibration technique for MEMS membrane type strain sensors. Presented at University/Government/Industry Microelectronics Symposium, 1999. Proceedings of the Thirteenth Biennial. 1999, .

[40] L. Cao, T. S. Kim, S. C. Mantell and D. L. Polla. Simulation and fabrication of piezoresistive membrane type MEMS strain sensors. *Sensors and Actuators A: Physical 80(3),* pp. 273-279. 2000. . DOI:http://dx.doi.org.login.ezproxy.library.ualberta.ca/10.1016/S0924-4247(99)00343-X.

[41] C. Hautamaki, L. Cao, J. Zhou, S. C. Mantell and T. S. Kim. Calibration of MEMS strain sensors fabricated on silicon: Theory and experiments. *Microelectromechanical Systems, Journal of 12(5),* pp. 720-727. 2003.

[42] C. Hautamaki, S. Zurn, S. C. Mantell and D. L. Polla. Experimental evaluation of MEMS strain sensors embedded in composites. *Microelectromechanical Systems, Journal of 8(3),* pp. 272-279. 1999.

[43] E. Hwang, Y. Kim and B. Ju. Flexible polysilicon sensor array modules using "etch-release" packaging scheme. *Sensors and Actuators A: Physical 111(1),* pp. 135-141. 2004. . DOI:http://dx.doi.org.login.ezproxy.library.ualberta.ca/10.1016/j.sna.2003.10.022.

[44] S. Kon, K. Oldham and R. Horowitz. Piezoresistive and piezoelectric MEMS strain sensors for vibration detection. Presented at The 14th International Symposium on: Smart Structures and Materials & Nondestructive Evaluation and Health Monitoring. 2007.

[45] Y. Kim, Y. Kim, C. Lee and S. Kwon. Thin polysilicon gauge for strain measurement of structural elements. *Sensors Journal, IEEE 10(8),* pp. 1320-1327. 2010.

[46] A. A. Mohammed, W. A. Moussa and E. Lou. Development and experimental evaluation of a novel piezoresistive MEMS strain sensor. *Sensors Journal, IEEE 11(10),* pp. 2220-2232. 2011.

[47] S. M. Won, H. Kim, N. Lu, D. Kim, C. Del Solar, T. Duenas, A. Ameen and J. A. Rogers. Piezoresistive strain sensors and multiplexed arrays using assemblies of single-crystalline silicon nanoribbons on plastic substrates. *Electron Devices, IEEE Transactions on 58(11),* pp. 4074-4078. 2011.

[48] A. A. Mohammed, W. A. Moussa and E. Lou. High-performance piezoresistive MEMS strain sensor with low thermal sensitivity. *Sensors 11(2),* pp. 1819-1846. 2011.

[49] http://www.sensorland.com/HowPage002.html

Appendix A: Sensor signal response at 0 Hz vibration (sensor conditioner's voltage signature)

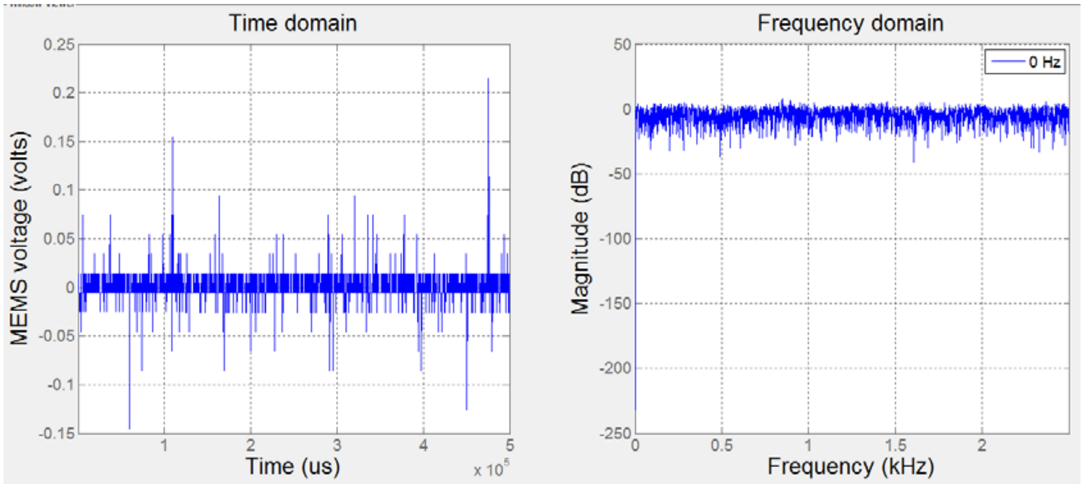

Figure A4: Time series and frequency response at 0 Hz vibration. Signal peaks are signature of the voltage source. The frequency domain representation of the time series is characteristic of white noise

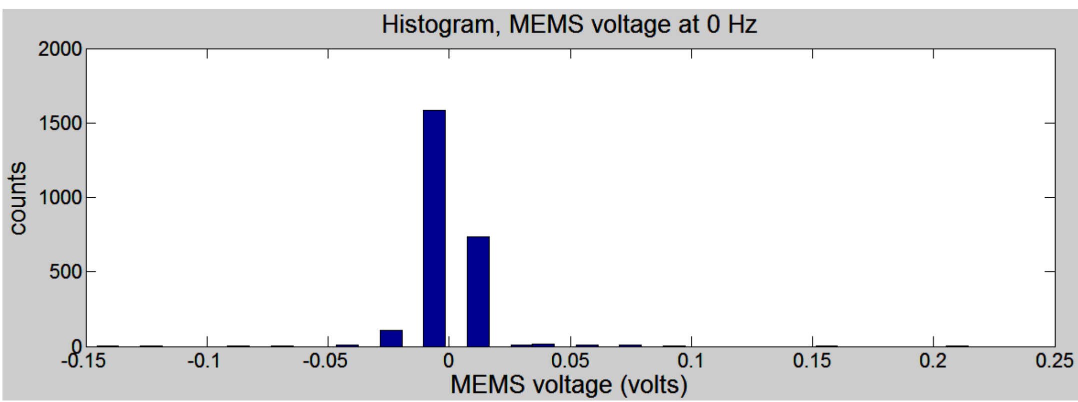

Figure A5: Distribution of the MEMS voltage at 0 Hz vibration.

Appendix B: Raw vibration data from 0 Hz to 220 Hz

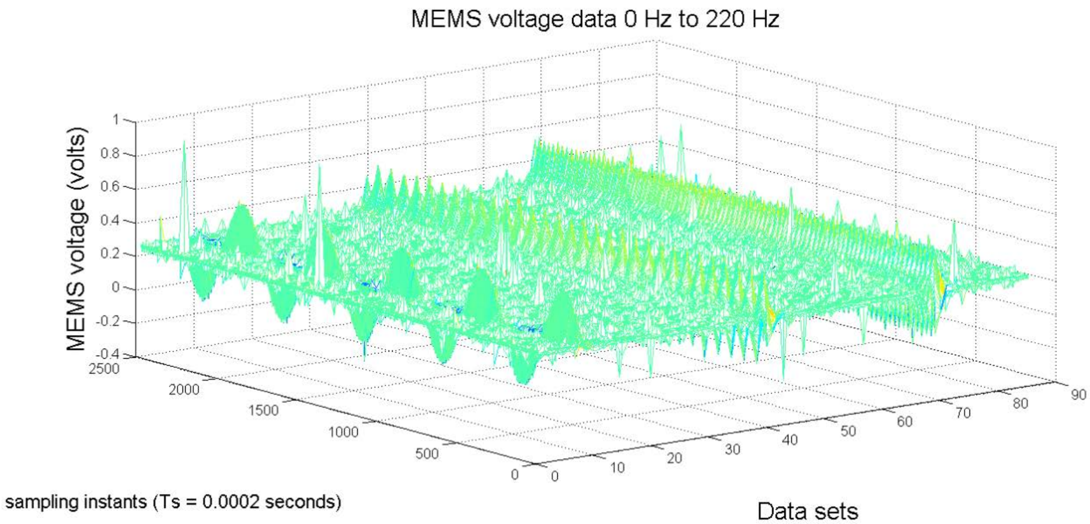

Figure B1: 3D plot of the raw data, MEMS voltage 0 Hz to 220 Hz data

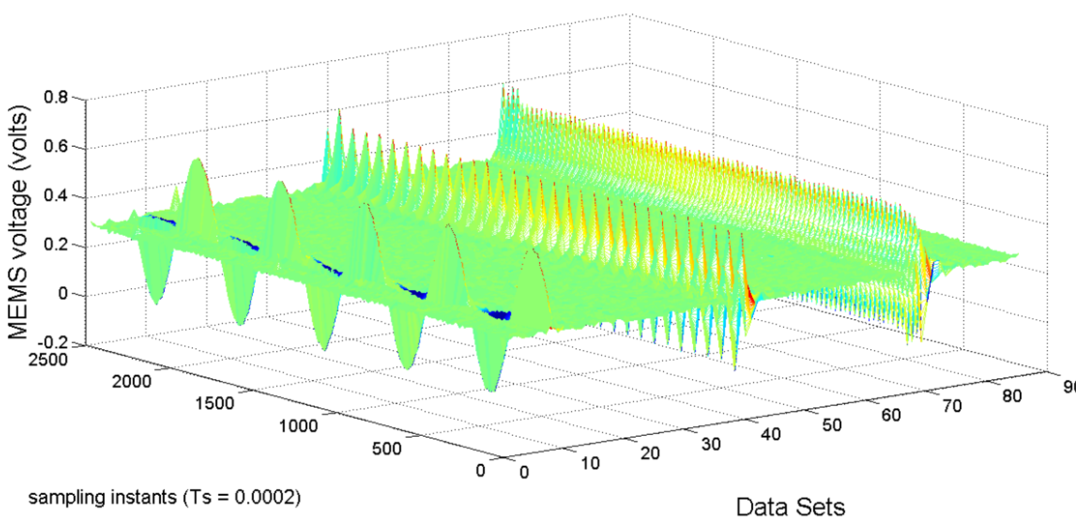

Figure B2: 3D plot of the filtered data (smoothed) MEMS voltage data 0 Hz to 220 Hz

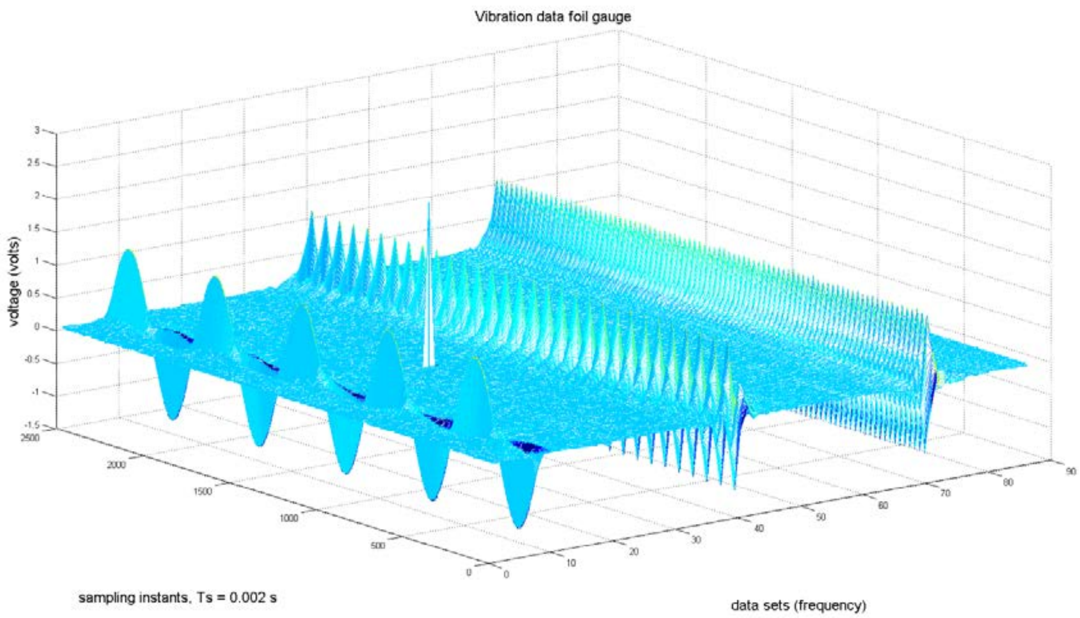

Figure B3: 3D plot of vibration data from foil gauge, 0 Hz to 220 Hz

Legend: Frequency and data set number designation

Data set 1 – 0 Hz	Data set 22 – 24 Hz	Data set 43 – 66 Hz	Data set 64 – 169 Hz
Data set 2 – 4 Hz	Data set 23 – 25 Hz	Data set 44 – 67 Hz	Data set 65 – 170 Hz
Data set 3 – 5 Hz	Data set 24 – 27 Hz	Data set 45 – 68 Hz	Data set 66 – 172 Hz
Data set 4 – 6 Hz	Data set 25 – 30 Hz	Data set 46 – 70 Hz	Data set 67 – 173 Hz
Data set 5 – 7 Hz	Data set 26 – 32 Hz	Data set 47 – 72 Hz	Data set 68 – 174 Hz
Data set 6 – 8 Hz	Data set 27 – 37 Hz	Data set 48 – 74 Hz	Data set 69 – 175 Hz
Data set 7 – 9 Hz	Data set 28 – 40 Hz	Data set 49 – 76 Hz	Data set 70 – 176 Hz
Data set 8 – 10 Hz	Data set 29 – 42 Hz	Data set 50 – 78 Hz	Data set 71 – 177 Hz
Data set 9 – 11 Hz	Data set 30 – 46 Hz	Data set 51 – 80 Hz	Data set 72 – 178 Hz
Data set 10 – 12 Hz	Data set 31 – 50 Hz	Data set 52 – 82 Hz	Data set 73 – 179 Hz
Data set 11 – 13 Hz	Data set 32 – 52 Hz	Data set 53 – 86 Hz	Data set 74 – 180 Hz
Data set 12 – 14 Hz	Data set 33 – 54 Hz	Data set 54 – 90 Hz	Data set 75 – 182 Hz
Data set 13 – 15 Hz	Data set 34 – 55 Hz	Data set 55 – 100 Hz	Data set 76 – 184 Hz
Data set 14 – 16 Hz	Data set 35 – 57 Hz	Data set 56 – 110 Hz	Data set 77 – 186 Hz
Data set 15 – 17 Hz	Data set 36 – 59 Hz	Data set 57 – 120 Hz	Data set 78 – 188 Hz
Data set 16 – 18 Hz	Data set 37 – 60 Hz	Data set 58 – 130 Hz	Data set 79 – 190 Hz
Data set 17 – 19 Hz	Data set 38 – 61 Hz	Data set 59 – 140 Hz	Data set 80 – 195 Hz
Data set 18 – 20 Hz	Data set 39 – 62 Hz	Data set 60 – 150 Hz	Data set 81 – 200 Hz
Data set 19 – 21 Hz	Data set 40 – 63 Hz	Data set 61 – 160 Hz	Data set 82 – 205 Hz
Data set 20 – 22 Hz	Data set 41 – 64 Hz	Data set 62 – 165 Hz	Data set 83 – 210 Hz
Data set 21 – 23 Hz	Data set 42 – 65 Hz	Data set 63 – 168 Hz	Data set 84 – 215 Hz

Appendix C: Sensor transient voltage, average power and voltage settling times obtained at different temperatures

Table 1: Loaded MEMS sensor, T = 80 ^{o}C

Current, mA	Voltage (mean ± SD), V	Power, W	Rise time, µs	Fall time, µs
2.35	0.1824336 ± 0.0058	0.000428719	173.5	159.1
2.37	0.1828864 ± 0.0024	0.000433441	168.2	161.8
2.36	0.1823968 ± 0.0078	0.000430456	192.6	161.8
2.36	0.1825792 ± 0.0057	0.000430887	157.4	169.4
2.36	0.182712 ± 0.0029	0.0004312	166.3	160
2.36	0.1823888 ± 0.0028	0.000430438	176.2	158.2
2.36	0.18224 ± 0.0027	0.000430086	268.9	167.4
2.34	0.1818336 ±0.0060	0.000425491	164	163.6
2.36	0.1817216 ± 0.0028	0.000428863	160.9	169.4
2.36	0.1816416 ± 0.0028	0.000428674	159.1	154.8
2.36	0.1813712 ± 0.0079	0.000428036	155.8	160
2.36	0.1816416 ±0.0058	0.000428674	160.9	160
2.36	0.1814928 ± 0.0024	0.000428323	164.4	163.6
2.36	0.1810512 ± 0.0068	0.000427281	310.8	156.5
2.36	0.1809504 ± 0.0024	0.000427043	164	156.5
2.36	0.1810272 ± 0.0026	0.000427224	162.6	158.2
2.36	0.1807648 ± 0.0059	0.000426605	178.3	160
2.35	0.180456 ± 0.0076	0.000424072	170.1	156.5
2.36	0.177592 ± 0.024	0.000419117	165.9	165.5
2.35	0.177344 ± 0.023	0.000416758	164.4	175.6
2.35	0.1771024 ± 0.023	0.000416191	162.2	158.2
2.35	0.177192 ± 0.023	0.000416401	165.9	163.6
2.35	0.1772016 ± 0.023	0.000416424	176.2	163.6
2.35	0.1768448 ± 0.023	0.000415585	165.9	236.7
2.35	0.1762704 ± 0.023	0.000414235	153.2	167.4
2.35	0.176112 ± 0.024	0.000413863	158.2	158.2
2.35	0.1761504 ± 0.023	0.000413953	169.4	163.6
2.35	0.1755952 ± 0.023	0.000412649	199.7	163.6
2.35	0.1758048 ± 0.023	0.000413141	162.2	158.2
2.35	0.1755328 ± 0.024	0.000412502	163.6	165.5

Table 2: Unloaded MEMS sensor, T = 80 ^{o}C

Current, mA	Voltage (mean ± SD), V	Power, W	Rise time, μs	Fall time, μs
2.34	0.09130944 ± 0.0041	0.000213664	181.5	171.7
2.34	0.09099456 ± 0.0041	0.000212927	179.8	160.3
2.34	0.09073664 ± 0.0056	0.000212324	281.3	148.8
2.33	0.09093568 ± 0.0046	0.00021188	464	160.8
2.33	0.09061056 ±0.0055	0.000211123	172.2	158.7
2.33	0.09091584 ± 0.0050	0.000211834	241.9	167
2.33	0.09075008 ± 0.0055	0.000211448	183.3	161.3
2.31	0.09097152 ± 0.0049	0.000210144	271.7	160.3
2.33	0.09106944 ± 0.0050	0.000212192	172.4	163.8
2.33	0.09111936 ± 0.0048	0.000212308	167.6	156.1
2.31	0.09116608 ± 0.0032	0.000210594	170.4	159
2.33	0.09118912 ± 0.0051	0.000212471	160.7	156.4
2.33	0.09100288 ± 0.0054	0.000212037	148.8	176.3
2.33	0.09114944 ± 0.0056	0.000212378	165	165.1
2.33	0.0914688 ± 0.0049	0.000213122	170.4	161.2
2.32	0.09144576 ± 0.0051	0.000212154	307.1	155.2
2.32	0.09164992 ± 0.0042	0.000212628	164.9	170.2
2.32	0.09173248 ± 0.0042	0.000212819	170.7	166.1
2.32	0.0917312 ± 0.0057	0.000212816	164.2	174.8
2.32	0.0915744 ± 0.0052	0.000212453	155.4	161.7
2.32	0.09161152 ± 0.0058	0.000212539	178.4	173.5
2.32	0.09164992 ± 0.0058	0.000212628	157.1	148.8
2.32	0.09194816 ± 0.0051	0.00021332	152.8	159.3
2.32	0.0922528 ± 0.0051	0.000214026	150.4	164.7
2.32	0.09197248 ± 0.0058	0.000213376	179	146.3
2.32	0.09223552 ± 0.0052	0.000213986	183.5	167.8
2.32	0.09261248 ± 0.0044	0.000214861	151.6	151.9
2.32	0.09265152 ± 0.0056	0.000214952	160	160.7
2.32	0.09262912 ± 0.0064	0.0002149	144.6	159.3
2.30	0.0928192 ± 0.0059	0.000213484	182.3	159.3

Table 3: Loaded MEMS sensor at T = -20 ^{o}C

Current, mA	Voltage (mean ± SD), V	Power, W	Rise time, μs	Fall time, μs
2.53	0.3118864 ± 0.019	0.000789073	86.99	80.79
2.53	0.3114144 ± 0.018	0.000787878	83.55	81.88
2.53	0.3116912 ± 0.018	0.000788579	87.67	84.72
2.53	0.3103632 ± 0.025	0.000785219	81.41	87.14
2.53	0.3110336 ± 0.020	0.000786915	85.33	83.1
2.53	0.3109776 ± 0.020	0.000786773	81.01	85.51
2.53	0.3100112 ± 0.020	0.000784328	80	84.29
2.53	0.3092064 ± 0.018	0.000782292	83.55	86.13
2.53	0.3097408 ± 0.016	0.000783644	84.56	90.08
2.54	0.3094688 ± 0.018	0.000786051	82.35	79.19
2.54	0.3087344 ± 0.020	0.000784185	84.11	83.1
2.54	0.3084992 ± 0.020	0.000783588	80.38	85.4
2.54	0.3078672 ± 0.018	0.000781983	88.11	82.99
2.54	0.3080416 ± 0.020	0.000782426	81.94	81.38
2.54	0.3074144 ± 0.018	0.000780833	81.17	81.94
2.54	0.3073904 ± 0.021	0.000780772	80.13	80.82
2.54	0.3083488 ± 0.018	0.000783206	87.5	86.13
2.54	0.3088208 ± 0.018	0.000784405	79.87	79.73
2.54	0.3090368 ± 0.020	0.000784953	86.39	80.69
2.54	0.3083888 ± 0.020	0.000783308	83.55	80.69
2.54	0.3082032 ± 0.020	0.000782836	89.44	87.31
2.54	0.3080736 ± 0.018	0.000782507	84.67	80.27
2.54	0.3079584 ± 0.018	0.000782214	82.89	81.94
2.54	0.307984 ± 0.018	0.000782279	80.77	83.1
2.54	0.3079632 ± 0.022	0.000782227	80.77	88.06
2.54	0.30852 ± 0.015	0.000783641	81.41	90.7
2.54	0.3078928 ± 0.016	0.000782048	88.11	84.29
2.54	0.3073952 ± 0.018	0.000780784	81.82	86.76
2.54	0.3073424 ± 0.020	0.00078065	85.71	82.52
2.54	0.3067696 ± 0.020	0.000779195	85.14	84.78

Table 4: Unloaded MEMS sensor T = -20 ^{o}C

Current, mA	Voltage (mean ± SD), V	Power, W	Rise time, μs	Fall time, μs
2.58	0.11633984 ± 0.0067	0.000300157	103.3	82.31
2.58	0.1158048 ± 0.0075	0.000298776	81.38	80.45
2.58	0.11539392 ± 0.0061	0.000297716	79.73	84.92
2.58	0.11491328 ± 0.0066	0.000296476	89.31	79.85
2.58	0.1146688 ± 0.0053	0.000295846	88.64	87.6
2.59	0.11387328 ± 0.0060	0.000294932	83.45	80.3
2.59	0.1130368 ± 0.0076	0.000292765	81.56	79.1
2.59	0.1123904 ± 0.0069	0.000291091	82.01	75.71
2.59	0.1121792 ± 0.0067	0.000290544	82.61	79.7
2.6	0.1119936 ± 0.0075	0.000291183	80.71	86.18
2.6	0.11148032 ± 0.0077	0.000289849	90.4	80.15
2.6	0.11042112 ± 0.0080	0.000287095	80	80.15
2.6	0.11041792 ± 0.0065	0.000287087	86.82	84
2.6	0.1101152 ± 0.0086	0.0002863	85.5	81.54
2.6	0.11005824 ± 0.0072	0.000286151	77.78	77.94
2.6	0.10964928 ± 0.0059	0.000285088	89.6	81.4
2.6	0.10954176 ± 0.0058	0.000284809	80	87.5
2.6	0.10886784 ± 0.0067	0.000283056	78.32	79.55
2.61	0.10874688 ± 0.0057	0.000283829	84.73	84
2.6	0.10812544 ± 0.0066	0.000281126	82.22	83.33
2.61	0.10850944 ± 0.0073	0.00028321	82.22	82.68
2.61	0.1084064 ± 0.0066	0.000282941	82.84	77.78
2.61	0.10805632 ± 0.0079	0.000282027	88.1	85.37
2.61	0.10797696 ± 0.0071	0.00028182	81.02	84
2.61	0.10755648 ± 0.0069	0.000280722	82.09	79.55
2.61	0.10757312 ± 0.0065	0.000280766	79.71	80.15
2.61	0.10738048 ± 0.0072	0.000280263	83.21	81.4
2.61	0.10704192 ± 0.0078	0.000279379	81.34	87.5
2.61	0.10675456 ± 0.0067	0.000278629	80.15	84.68
2.61	0.10632512 ± 0.0086	0.000277509	81.95	83.87

Table 5 Loaded MEMS sensor T = 24 ^{o}C

Current, mA	Voltage (mean ± SD), V	Power, W	Rise time, μs	Fall time, μs
2.52	0.1963568 ± 0.0012	0.000494819	162.9	156.4
2.52	0.196304 ± 0.0012	0.000494819	159.6	156.4
2.52	0.196368 ± 0.0012	0.000494847	175.6	158
2.52	0.196224 ± 0.0058	0.000494484	166.3	158
2.52	0.1963968 ± 0.0011	0.00049492	158	161.2
2.52	0.1963936 ± 0.0012	0.000494912	168.1	159.6
2.52	0.1962608 ± 0.0019	0.000494577	517.3	159.6
2.52	0.1961856 ± 0.0011	0.000494388	156.4	161.2
2.52	0.195936 ± 0.0011	0.000493759	164.6	159.6
2.52	0.1957744 ± 0.0058	0.000493351	158	161.2
2.52	0.1958848 ± 0.0011	0.00049363	166.3	158
2.52	0.1958992 ± 0.0011	0.000493666	245	159.6
2.52	0.1959536 ± 0.0012	0.000493803	166.3	161.2
2.52	0.1960752 ± 0.0011	0.00049411	164.6	159.6
2.52	0.196216 ± 0.0011	0.000494464	161.2	158
2.52	0.1963136 ± 0.0011	0.00049471	162.9	158
2.52	0.1963856 ± 0.0012	0.000494892	164.6	158
2.52	0.1963744 ± 0.0011	0.000494863	158	158
2.52	0.196336 ± 0.0013	0.000494767	158.4	158
2.52	0.1962464 ± 0.0011	0.000494541	160	158
2.52	0.1962288 ± 0.0011	0.000494497	160	159.6
2.52	0.1961904 ± 0.0012	0.0004944	262	160
2.52	0.1961168 ± 0.0011	0.000494214	161.2	163.3
2.52	0.1960144 ± 0.0011	0.000493956	159.6	168.4
2.52	0.1959696 ± 0.0019	0.000493843	162.9	160
2.52	0.1960544 ± 0.0011	0.000494057	168.1	164.9
2.52	0.1959968 ± 0.0011	0.000493912	168.1	166.7
2.52	0.1959456 ± 0.0011	0.000493783	162.9	163.3
2.52	0.1957648 ± 0.0011	0.000493327	158	161.6
2.52	0.1957232 ± 0.0011	0.000493222	159.6	163.3
2.52	0.1958816 ± 0.0011	0.000493622	161.2	163

Table 6: Unloaded MEMS sensor, T = 24 ^{o}C

Current, mA	Voltage (mean ± SD), V	Power, W	Rise time, μs	Fall time, μs
2.48	0.107691914 ± 0.0032	0.000267076	163.2	166
2.48	0.107641313 ± 0.0032	0.00026695	161.8	164.5
2.48	0.107823219 ± 0.0009	0.000267402	162	161.5
2.48	0.107777742 ± 0.0013	0.000267289	160.6	166
2.48	0.107965412 ± 0.0009	0.000267754	162	160
2.48	0.108023699 ± 0.0009	0.000267899	168.2	157.1
2.48	0.107913531 ± 0.0010	0.000267626	163.2	164.5
2.48	0.107757246 ± 0.0033	0.000267238	163.2	167.6
2.48	0.107909688 ± 0.0010	0.000267616	162	161.5
2.48	0.107793755 ± 0.0009	0.000267329	162	163
2.48	0.107748279 ± 0.0029	0.000267216	162	163
2.48	0.108016653 ± 0.0010	0.000267881	166.9	163
2.48	0.107884708 ± 0.0010	0.000267554	169.5	161.1
2.48	0.107959648 ± 0.0009	0.00026774	162	164.5
2.48	0.107809127 ± 0.0009	0.000267367	169.5	160
2.48	0.107864852 ± 0.0045	0.000267505	164.4	161.5
2.48	0.107918655 ± 0.0010	0.000267638	163.2	163
2.48	0.107991673 ± 0.0010	0.000267819	163.2	161.5
2.48	0.107902642 ± 0.0010	0.000267599	164.4	169.2
2.48	0.107904564 ± 0.0009	0.000267603	159.7	166
2.48	0.107928903 ± 0.0009	0.000267664	160.9	177.8
2.48	0.107836029 ± 0.0033	0.000267433	177.6	164.5
2.48	0.107702162 ± 0.0032	0.000267101	165.7	164.5
2.48	0.107909688 ± 0.0009	0.000267616	162	161.5
2.48	0.107929544 ± 0.0010	0.000267665	159.4	160
2.48	0.107875741 ± 0.0010	0.000267532	164.4	157.1
2.48	0.107918655 ± 0.0010	0.000267638	174.8	161.5
2.48	0.107867414 ± 0.0010	0.000267511	163.2	163
2.48	0.107780945 ± 0.0033	0.000267297	159.7	164.5
2.48	0.107523459 ± 0.0054	0.000266658	169.2	161.5

Appendix D: Strain histories and cycle counting results from Scanimetrics Motescan v. 2.38.1

File Name	NumCycles	Eq.Strain
Foil Gauge	87	1261.76
MEMS Raw	100	1273.18
MEMS Filtered	86.5	1203.94

* Rainflow calculation criteria: 20 bins, 50 Microstrain as threshold

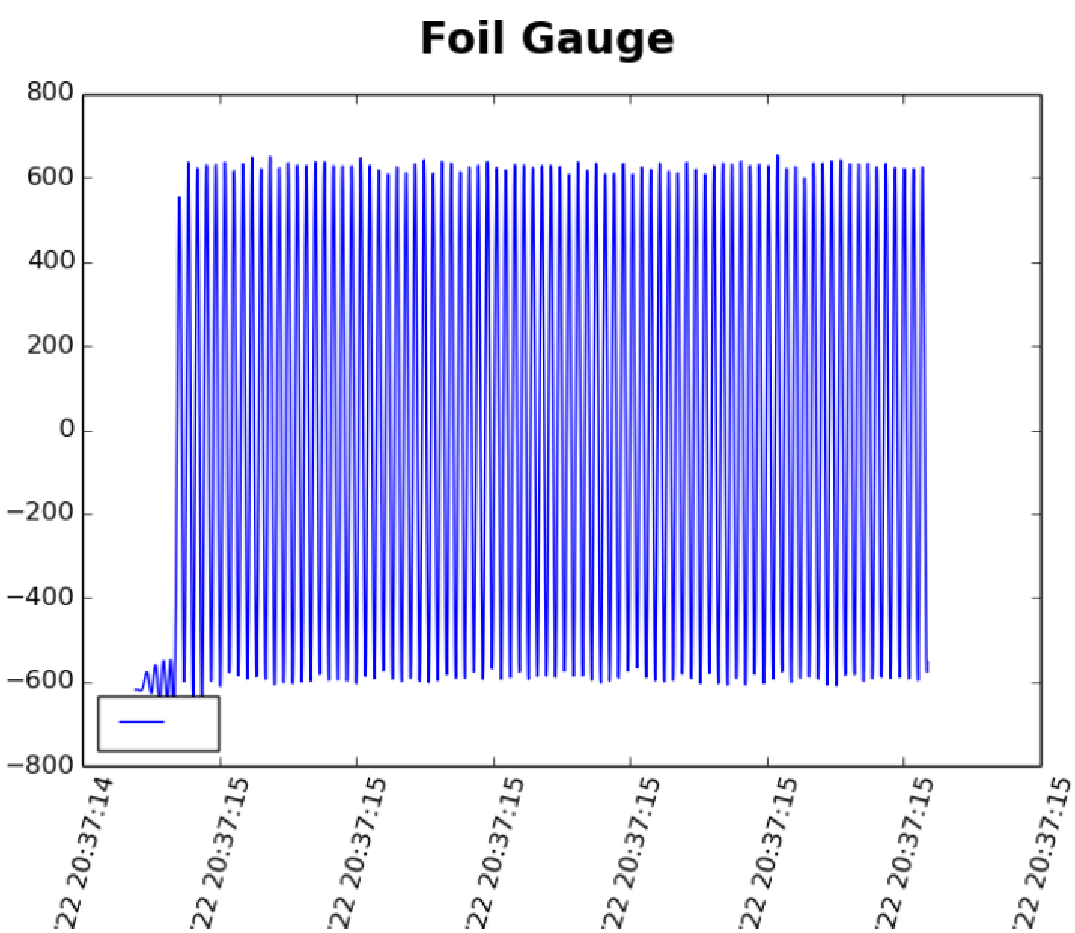

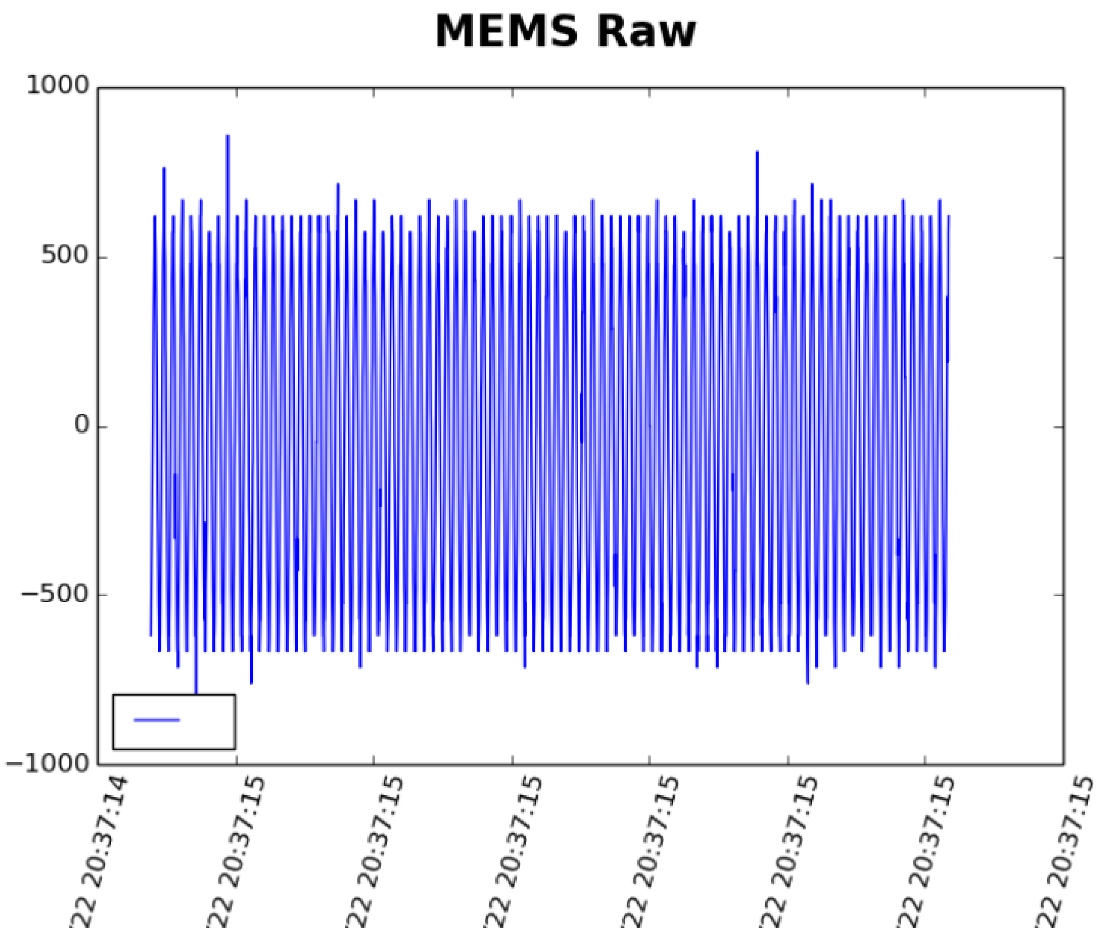
MEMS Raw
1000
500
0
−500
−1000
'22 20:37:14
'22 20:37:15
'22 20:37:15
'22 20:37:15
'22 20:37:15
'22 20:37:15
'22 20:37:15
'22 20:37:15

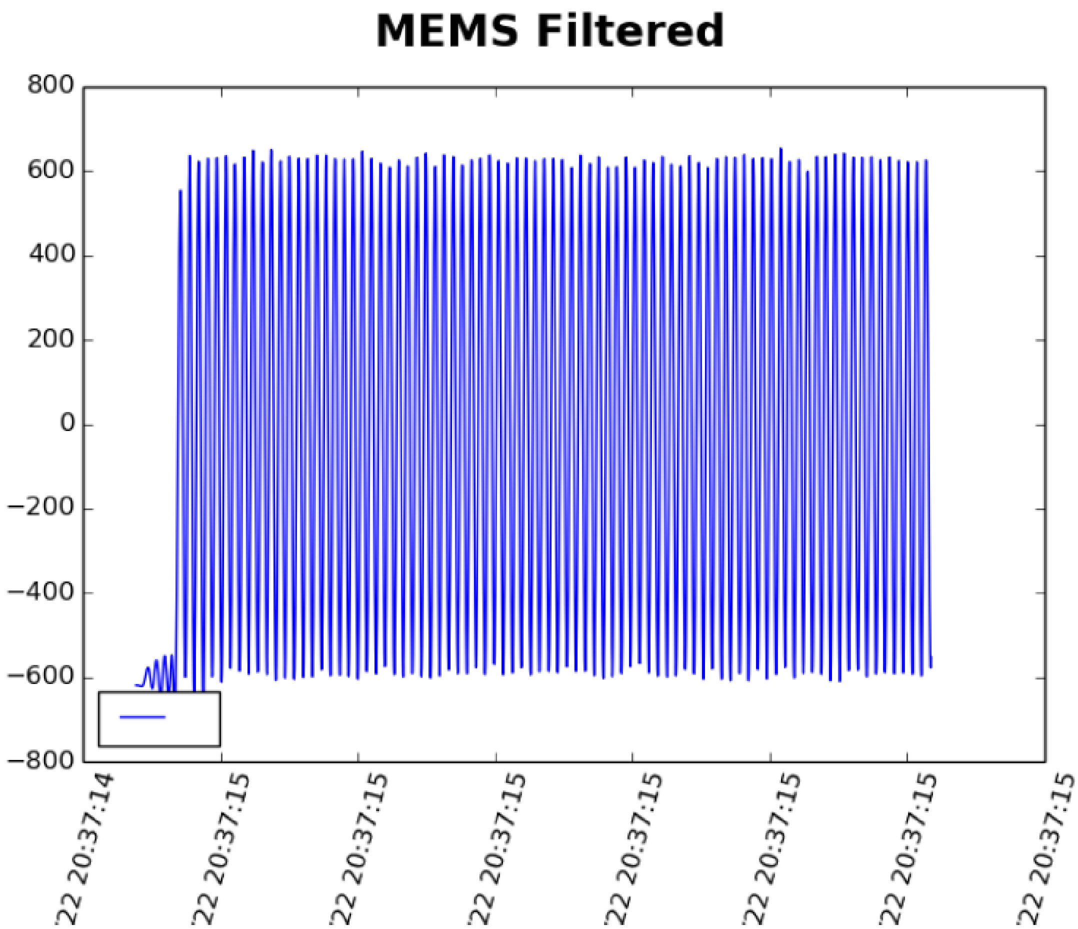
MEMS Filtered
800
600
400
200
0
−200
−400
−600
−800
'22 20:37:14
'22 20:37:15
'22 20:37:15
'22 20:37:15
'22 20:37:15
'22 20:37:15
'22 20:37:15
'22 20:37:15